

# Self-Supervised AI-Generated Image Detection: A Camera Metadata Perspective

Nan Zhong, Mian Zou, Yiran Xu, Zhenxing Qian, *Senior Member, IEEE*, Xinpeng Zhang, *Senior Member, IEEE*, Baoyuan Wu, *Senior Member, IEEE*, and Kede Ma, *Senior Member, IEEE*

**Abstract**—The proliferation of AI-generated imagery poses escalating challenges for multimedia forensics, yet many existing detectors depend on assumptions about the internals of specific generative models, limiting their cross-model applicability. We introduce a self-supervised approach for detecting AI-generated images that leverages camera metadata—specifically exchangeable image file format (EXIF) tags—to learn features intrinsic to digital photography. Our pretext task trains a feature extractor solely on camera-captured photographs by classifying categorical EXIF tags (e.g., camera model and scene type) and pairwise-ranking ordinal and continuous EXIF tags (e.g., focal length and aperture value). Using these EXIF-induced features, we first perform one-class detection by modeling the distribution of photographic images with a Gaussian mixture model and flagging low-likelihood samples as AI-generated. We then extend to binary detection that treats the learned extractor as a strong regularizer for a classifier of the same architecture, operating on high-frequency residuals from spatially scrambled patches. Extensive experiments across various generative models demonstrate that our EXIF-induced detectors substantially advance the state of the art, delivering strong generalization to in-the-wild samples and robustness to common benign image perturbations.

**Index Terms**—AI-generated image detection, self-supervised learning, image forensics.

## 1 INTRODUCTION

AI image generators, spanning autoregressive models [1], [2], variational autoencoders [3], normalizing flows [4], generative adversarial networks (GANs) [5]–[7], and diffusion models [8]–[10], now produce visuals that are widely used but also easily misused. Beyond creative applications, AI-generated imagery can facilitate harassment [11], fraud [12], and large-scale misinformation [13], underscoring the need to reliably distinguish camera-captured photographs from AI outputs<sup>1</sup>.

Much of today’s progress in AI-generated image detection hinges on model-aware assumptions. For example, methods targeting GANs often exploit upsampling artifacts in spatial [16] or frequency [17] domains, where diffusion-oriented approaches invert or approximate the denoising

trajectory and inspect reconstruction errors, similarly in spatial [18] or latent [19] domains. While effective in-family, such strategies generalize poorly across the rapidly diversifying space of generators and training pipelines.

A more durable route is to avoid learning “the space of fakes” altogether [20]. Ideally, a detector should be trained only on photographs, treating AI-generated images as out-of-distribution anomalies [21], [22] (also known as one-class classification). Prior related lines of work show promise: projecting into a fixed, semantics-oriented feature space [23], checking exchangeable image file format (EXIF) self-consistency across patches [20], and aligning photographic images with EXIF viewed as language via contrastive joint embedding [24]. However, semantic encoders mainly capture high-level associations, while EXIF–language alignment emphasizes cross-patch coherence for splicing; none fully exploit the fine-grained, camera-intrinsic regularities of image formation needed in AI-generated image detection.

In this work, we advocate a self-supervised perspective on EXIF-induced AI-generated image detection. Our key idea is to train a feature extractor from photographic images by predicting camera metadata: multi-class classification for categorical tags (e.g., Make, Model, and SceneCaptureType) and pairwise ranking [25] for ordinal and continuous tags (e.g., FocalLength and ApertureValue). To emphasize camera-intrinsic characteristics over semantics, the feature extractor operates on high-frequency residuals [26] of spatially scrambled patches. This pretext task aims to align the learned features with the physics and camera configurations of digital photography, without relying on any AI-generated examples.

Using the resulting EXIF-induced feature extractor, we instantiate two detectors. The first is a one-class model,

*This work was supported in part by the Hong Kong RGC General Research Fund (11220224), the CityU Strategic Research Grants (7005848 and 7005983), and the Guangdong Basic and Applied Basic Research Foundation (2024B1515020095).*

- Nan Zhong and Mian Zou are with the Department of Computer Science, City University of Hong Kong, Kowloon, Hong Kong (e-mail: nzhong@cityu.edu.hk, mianzou2-c@my.cityu.edu.hk).
- Yiran Xu, Zhenxing Qian, and Xinpeng Zhang are with the Department of Computer Science, Fudan University, Shanghai, 200433, China (e-mail: {yirxu23, zqxian, zhangxinpeng}@fudan.edu.cn).
- Baoyuan Wu is with the School of Artificial Intelligence, The Chinese University of Hong Kong, Shenzhen, Guangdong, 518172, China (email: wubaoyuan@cuhk.edu.cn).
- Kede Ma is with the Department of Computer Science and the Shenzhen Research Institute, City University of Hong Kong, Kowloon, Hong Kong (e-mail: kede.ma@cityu.edu.hk).

Corresponding Author: Kede Ma.

1. In this work, we refrain from labeling images as “real” or “fake” when contrasting photographic and AI-generated imagery, as contemporary generative models can memorize and reproduce photographs from their training data [14], [15].

SDAIE ( Self-supervised Detection of AI-generated Images using EXIF metadata), which fits a Gaussian mixture model (GMM) to photographic features and flags low-likelihood samples as AI-generated. The second, SDAIE<sup>†</sup>, is a binary classifier trained with ProGAN [6] images as a provisional negative class. A representation-alignment regularizer [27] ties its intermediate features to the pretext extractor, transferring camera-intrinsic cues and mitigating overfitting to the specified generator. Together, these yield strong performance across diverse generators, including in-the-wild samples from commercial APIs (*e.g.*, Midjourney [28]), and show robustness under benign post-processing.

In summary, our contributions include

- A self-supervised pretext task that leverages EXIF tags to learn camera-intrinsic features from photographs only;
- A feature extractor that operates on high-frequency residuals of scrambled patches to suppress semantics and accentuate imaging regularities;
- A one-class detector that models photographic features with a GMM and detects anomalies without seeing AI-generated images during training;
- A binary detector that uses the pretext extractor as a strong regularizer, improving generalization and robustness across generators and post-processing.

## 2 RELATED WORK

In this section, we provide an overview of research topics closely related to ours, including deep generative models, AI-generated image detection, self-supervised learning, and EXIF metadata for computer vision.

### 2.1 Deep Generative Models

Over the past decade, a broad family of deep generative models has emerged, leveraging a wide range of techniques including autoregression [1], [2], variational inference [3], invertible flow (*i.e.*, Gaussianization) [4], adversarial training [5]–[7], score matching [29], and stochastic processes [10]. Among these, GAN-based and diffusion-based models have garnered particular attention for their state-of-the-art image synthesis performance.

GANs [5] pit a generator against a discriminator in a minmax game. Early training was notoriously fragile, with model collapse, sensitivity to hyperparameters, and unclear progress evaluation. Several advances improved diversity and stability: replacing the Jensen-Shannon divergence with the Wasserstein distance [30], introducing minibatch discrimination [31], and enforcing Lipschitz continuity via spectral normalization [32] or gradient penalties [33]. Quantitative metrics such as Fréchet inception distance [34], inception score [31], and distributional precision and recall helped track progress despite limitations. Scaling to high resolutions typically follows a coarse-to-fine recipe, exemplified by progressive growing [6], sometimes complemented by super-resolution post-processing. Conditional GANs further enable controllable generation from class labels [35], [36], text prompts [37]–[39], or various forms of auxiliary images [40].

More recently, diffusion models [10] have become the default choice for high-quality, diverse, and stable image synthesis, supported by theoretical insights from score-based modeling [41]. An image is gradually perturbed to near-white noise in a forward noising process, while a neural network (typically a U-Net [42]) is trained to reverse this process step by step. The major practical bottleneck is slow sampling, which has sparked extensive acceleration efforts, including deterministic samplers with input skip connections [43], trajectory distillation [44]–[46], feature reuse [47], high-order solvers [48], parallel sampling [49], and learned sampler optimization [50]. High-resolution synthesis is commonly achieved with latent diffusion [51], [52], where control signals can be injected via input concatenation, cross-attention, or adaptive normalization. The resulting capabilities have driven the widespread availability of commercial image generation APIs [28], [53], allowing non-experts to produce images from text alone and underscoring the urgent need for reliable detectors of AI-generated imagery.

### 2.2 AI-Generated Image Detection

In step with advances in image generation, early detection techniques focused primarily on GAN-generated content. Durall *et al.* [54] showed that up-convolution layers, necessary to many generators, introduce spectrum aliasing that distinguishes synthetic from photographic images. Wang *et al.* [55] further found that a straightforward ResNet-50, trained on photographs and ProGAN [6] outputs, with simple augmentations (*i.e.*, JPEG compression and Gaussian blurring), transfers well across multiple GAN datasets. Marra *et al.* [56] observed that architectural choices, training data, and initialization seeds imprint distinctive “fingerprints” exploitable for detection and attribution [57]. However, detectors tailored to GAN artifacts often underperform on high-quality images from diffusion models. To bridge this gap, diffusion-oriented approaches have emerged [18], [19], [58], [59]. For instance, DIRE [18] and SeDID [60] leverage reconstruction errors via diffusion inversion, while DRCT [61] incorporates reconstructed images as hard negative samples. Overall, these lines of work chiefly target artifacts tied to a single model family; as generators evolve, those artifacts drift, diminishing detection reliability.

A parallel thread seeks some forms of universal fingerprints that generalize across a broad range of generative models, including GANs and diffusion models [18], [62], [63]. Liu *et al.* [62] treated high-frequency noise in photographs, extracted with a pre-trained denoiser, as universal cues; Tan *et al.* [63] pursued a related idea using input gradients of a pre-trained classifier. Ojha *et al.* [23] relied solely on CLIP image embeddings with nearest neighbor classification and linear probing. While these strategies improve cross-model generalization, their reliance on semantics-oriented pre-trained encoders limits sensitivity to camera-related cues, particularly for photorealistic diffusion-generated images. We instead introduce a self-supervised approach that learns to classify and rank EXIF metadata associated with photographs, yielding generator-agnostic, EXIF-induced features intrinsic to digital photography for AI-generated image detection.

### 2.3 Self-Supervised Learning

Self-supervised representation learning [64], defined as learning without human-provided labels, has become a central paradigm in computer vision. The goal is to train feature extractors that convert raw data into useful representations, thereby simplifying downstream tasks. Arguably, the most important design choice is the pretext task, with prominent families including structural alignment [65]–[68], clustering [69], contrastive learning (*e.g.*, instance discrimination [70], [71] and multi-view learning [72], [73]), masked prediction [74]–[76], cross-modal alignment [77], [78], and generative modeling [79].

In image forensics, Huh *et al.* [20] detected splicing by testing whether patches within an image share a single imaging pipeline (*i.e.*, exhibit consistent EXIF tags). Zheng *et al.* [24] advanced this idea by learning a joint embedding between image patches and EXIF metadata, treating the latter as a language-like modality. However, standard text tokenizers struggle to encode numerical relationships partly due to token fragmentation, which can limit the effectiveness of EXIF-induced feature learning. In this work, we exploit EXIF information more directly and at finer granularity to train the feature extractor that underpins our detectors, enabling both one-class and binary classification for AI-generated image detection.

### 2.4 EXIF Metadata for Computer Vision

EXIF is a standardized schema for embedding metadata in image files, providing information about both the imaging device and the capture conditions. Tags such as Make, Model, and Software identify the camera manufacturer, specific model, and any post-processing pipeline. Exposure-related tags (*e.g.*, ShutterSpeedValue, ApertureValue, and ISO) record exposure settings with associated motion characteristics. Geotags (*e.g.*, GPSLatitude and GPSLongitude) localize the capture and supply scene context. Temporal tags (*e.g.*, DateTimeOriginal and SubSecTimeOriginal) provide precise timestamps, revealing coarse context such as time of day and seasonality. The Flash tag indicates whether and how the flash fired, revealing artificial illumination or low-light conditions. Historically, EXIF has supported camera calibration [80] and has been leveraged for image quality assessment [81] and image splicing detection [20], [82]. We build on this line of work by exploiting EXIF-induced self-supervised learning for a distinct forensic objective—detecting AI-generated imagery.

## 3 PROPOSED METHODS

We present SDAIE—Self-supervised Detection of AI-generated Images using EXIF metadata. Our central idea is to learn a camera-intrinsic feature extractor (see Fig. 1) only from photographs by predicting their EXIF tags. We then detect AI-generated images as distributional outliers (one-class setting) or via a supervised binary detector regularized by the self-supervised features. This section details the pretext task, the feature extractor, and two detectors built atop the learned representations.

TABLE 1  
Selected EXIF tags for the pretext task.

Tag	Type	Example Value
Flash	Categorical	Flashfired, Flashauto
Make	Categorical	Canon, FUJIFILM
MeteringMode	Categorical	Multi-segment, Spot
Model	Categorical	EOS5DMarkII, EOS7D
SceneCaptureType	Categorical	Standard, Landscape
ExposureMode	Categorical	Auto, Manual
WhiteBalanceMode	Categorical	Auto, Manual
ExposureBiasValue	Ordinal	0 EV, -1 EV
ISOSpeedRatings	Ordinal	400, 100
ApertureValue	Continuous	F2.8, F4
ExposureTime	Continuous	1/60 sec, 1/200 sec
F-Number	Continuous	F2.0, F3.2
FocalLength	Continuous	24 mm, 35 mm
ShutterSpeedValue	Continuous	1/60 sec, 1/100 sec

### 3.1 Pretext Task

Modern generators are capable of closely mimicking photographic semantics, so we deliberately avoid semantics and instead align features with imaging regularities recorded in EXIF. From more than one hundred EXIF tags, we retain *fourteen* informative ones with manageable missing rates and high entropy: seven categorical, two ordinal, and five continuous (see Table 1).

For each categorical tag  $i$ , we attach a lightweight head  $g(\cdot; \phi_i)$ , parameterized by  $\phi_i$ , to a shared feature extractor  $f(\cdot; \theta)$ , parameterized by  $\theta$ , and optimize the cross-entropy loss to predict among the most frequent categories, collapsing the long tail into the “others” category:

$$\ell_{\text{cat}}(\mathbf{x}; \theta, \phi_i) = - \sum_{j=1}^{C_i} p_{ij}(\mathbf{x}) \log(\sigma_j(g \circ f(\mathbf{x}; \theta, \phi_i))), \quad (1)$$

where

$$\sigma_j(\mathbf{z}) = \frac{\exp(z_j)}{\sum_{k=1}^{C_i} \exp(z_k)}. \quad (2)$$

Here  $C_i$  is the number of categories for the  $i$ -th EXIF tag, and  $p_{ij}(\mathbf{x}) \in \{0, 1\}$  represents a one-hot indicator that equals one if the ground-truth category of tag  $i$  for photographic image  $\mathbf{x}$  is  $j$ . The consolidation of infrequent categories combats heavy class imbalance while preserving discriminative information.

For each ordinal/continuous tag  $i$ , we eschew direct regression and instead learn pairwise rankings: given two photos  $\mathbf{x}$  and  $\mathbf{y}$  with  $i$ -th tag values  $s_i(\mathbf{x})$  and  $s_i(\mathbf{y})$ , we predict whether  $s_i(\mathbf{x}) \geq s_i(\mathbf{y})$ :

$$p_i(\mathbf{x}, \mathbf{y}) = \begin{cases} 1 & s_i(\mathbf{x}) \geq s_i(\mathbf{y}) \\ 0 & \text{otherwise.} \end{cases} \quad (3)$$

Using Thurstone’s model [83], the predicted probability reduces to a standard Gaussian cumulative distribution function  $\Phi(\cdot)$  of the score difference from a scalar prediction head  $g(\cdot; \varphi_i)$ :

$$\begin{aligned} p(\mathbf{x}, \mathbf{y}; \theta, \varphi_i) &= \Pr(g \circ f(\mathbf{x}; \theta, \varphi_i) \geq g \circ f(\mathbf{y}; \theta, \varphi_i)) \\ &= \Phi\left(\frac{g \circ f(\mathbf{x}; \theta, \varphi_i) - g \circ f(\mathbf{y}; \theta, \varphi_i)}{\sqrt{2}}\right), \end{aligned} \quad (4)$$

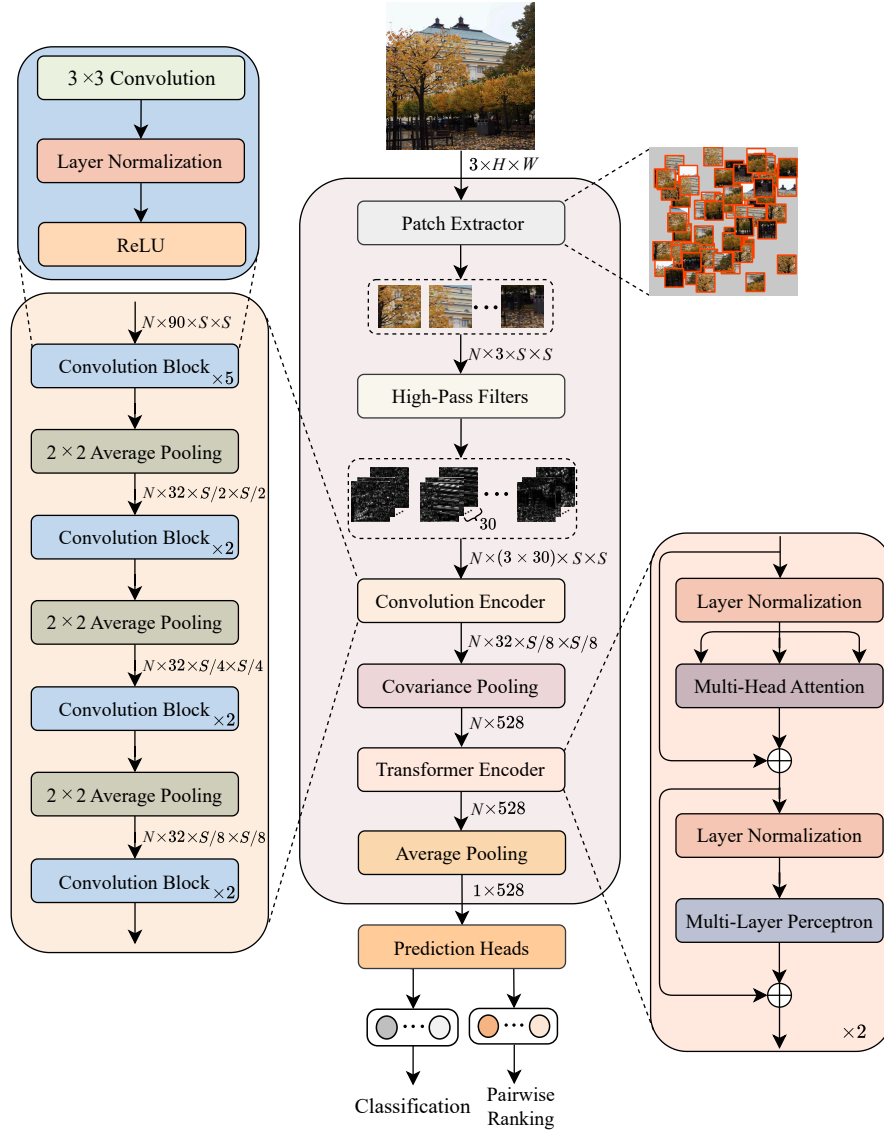


Fig. 1. System diagram of the proposed feature extractor using residual patch encoding, covariance pooling, and Transformer attention, trained solely on photographic images with EXIF metadata.

where we fix the variance parameter to one (corresponding to Thurstone’s Case V model). As with categorical tags, we adopt the cross-entropy loss for optimization:

$$\begin{aligned} \ell_{\text{rank}}(\mathbf{x}, \mathbf{y}; \boldsymbol{\theta}, \boldsymbol{\varphi}_i) = & -p_i(\mathbf{x}, \mathbf{y}) \log(p(\mathbf{x}, \mathbf{y}; \boldsymbol{\theta}, \boldsymbol{\varphi}_i)) \\ & - (1 - p_i(\mathbf{x}, \mathbf{y})) \log(1 - p(\mathbf{x}, \mathbf{y}; \boldsymbol{\theta}, \boldsymbol{\varphi}_i)). \end{aligned} \quad (5)$$

Notably, this ranking formulation is fairly robust to uneven spacings and mis-specified quantization, typical of EXIF numerics. The total pretext objective linearly combines tag-wise classification and pairwise ranking losses:

$$\begin{aligned} \ell(\mathcal{B}; \boldsymbol{\theta}, \boldsymbol{\phi}, \boldsymbol{\varphi}) = & \frac{1}{|\mathcal{B}|} \sum_{\mathbf{x} \in \mathcal{B}} \sum_i \alpha_i \ell_{\text{cat}}(\mathbf{x}; \boldsymbol{\theta}, \boldsymbol{\phi}_i) \\ & + \frac{1}{\binom{|\mathcal{B}|}{2}} \sum_{(\mathbf{x}, \mathbf{y}) \in \mathcal{B}} \sum_i \beta_i \ell_{\text{rank}}(\mathbf{x}, \mathbf{y}; \boldsymbol{\theta}, \boldsymbol{\varphi}_i), \end{aligned} \quad (6)$$

where  $\mathcal{B}$  is a minibatch of photographic images,  $i$  indexes EXIF tags, and  $\{\alpha, \beta\}$  are predetermined weighting vectors.

### 3.2 Network Architecture Design

AI-generated image detection—a specialized task in image forensics—relies less on image semantics and more on camera-intrinsic, low-level cues that directly inform image synthesis. To emphasize such cues, given a photographic image  $\mathbf{x} \in \mathbb{R}^{3 \times H \times W}$ , we first extract multiple (and possibly overlapping) patches  $\mathbf{X} \in \mathbb{R}^{N \times 3 \times S \times S}$ , where  $(H, W)$  and  $(S, S)$  denote the image and patch sizes, and  $N$  is the number of extracted patches. We intentionally discard patch coordinates (*i.e.*, no positional embeddings [84]), producing a patch-scrambling effect that disrupts scene structure and reduces the utility of high-level context. Consistent with perceptual and psychophysical findings [85], [86], such scrambling shifts reliance toward low-level features like color and texture to make sense of scene structure. To further emphasize forensic microstructures rather than semantics, we apply the high-pass filters of Fridrich and Kodovský [26] to each patch (see Fig. 2), amplifying residual signals that

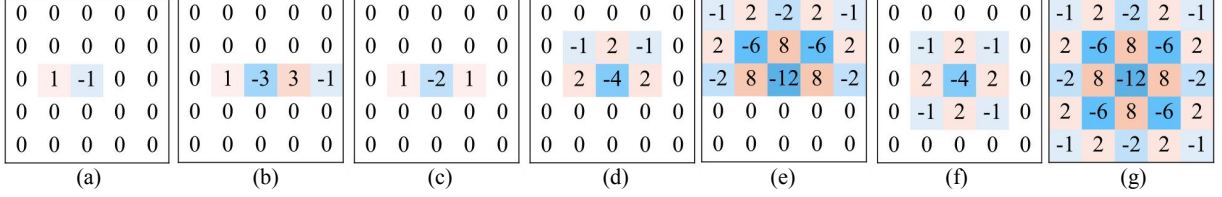


Fig. 2. Seven prototype kernels for constructing the high-pass filter bank via discrete rotations. (a) and (b) are rotated to eight compass directions  $\{\nearrow, \rightarrow, \searrow, \downarrow, \swarrow, \leftarrow, \nwarrow, \uparrow\}$ ; (c) is rotated to four directions  $\{\rightarrow, \downarrow, \nearrow, \swarrow\}$  (opposite directions are equivalent); (d) and (e) are rotated to the four cardinal directions  $\{\rightarrow, \downarrow, \leftarrow, \uparrow\}$ ; and (f) and (g) are used without rotation. In total, this yields 30 high-pass filters ( $2 \times 8 + 1 \times 4 + 2 \times 4 + 2$ ).

carry traces of the in-camera pipeline, including sensor noise and photo-response non-uniformity, color filter array demosaicing periodicity, lens sharpening, and compression footprints. The filtered patches are then passed through several stages of convolution, layer normalization, ReLU activation, and  $2 \times 2$  average pooling to extract local features.

After convolution encoding, we summarize patch features with covariance pooling [87] rather than average pooling. This is because average pooling primarily captures first-order statistics (*i.e.*, means), which are weak or near-zero in high-pass residuals and thus poorly informative. In contrast, covariance pooling preserves second-order structure that is more stable to global luminance/contrast shifts and semantic changes than means. Moreover, these second-order cues better capture the “texture of residuals” that separates digital acquisition from synthesis. Finally, we apply a Transformer encoder with self-attention across patches to model long-range interactions, followed by average pooling, yielding a 528-dimensional feature representation.

During training, we append fourteen lightweight prediction heads, each implemented by a fully connected layer corresponding to classification or ranking objectives for individual EXIF tags. These heads are used only for pretext supervision and are discarded at test time for AI-generated image detection. Fig. 3 compares t-SNE embeddings [88] of features from CLIP [77] and from our EXIF-induced extractor for photographic images versus those generated by SDXL [51], Midjourney [28], and DALLE2 [53]. Due to their photorealism and semantic richness, AI-generated images cluster near photographic images in the CLIP space. In contrast, our EXIF-induced features produce a clear separation between the two domains, a notable result given that the feature extractor is trained exclusively on photographs.

### 3.3 SDAIE

In this subsection, we address the problem of flagging AI-generated images as anomalies when only photographic images are available for training (see Fig. 4(a)). Let  $\mathbf{v}$  denote the EXIF-induced feature vector of a photographic image. We model the feature distribution with a GMM [89], which is expressive (with mixtures capturing multi-modal device/setting/shooting variability), interpretable (with component means/covariances), and probabilistic (enabling principled uncertainty and outlier scoring):

$$p(\mathbf{v}; \boldsymbol{\omega}) = \sum_{k=1}^K \pi_k \mathcal{N}(\mathbf{v}; \boldsymbol{\mu}_k, \boldsymbol{\Sigma}_k), \quad (7)$$

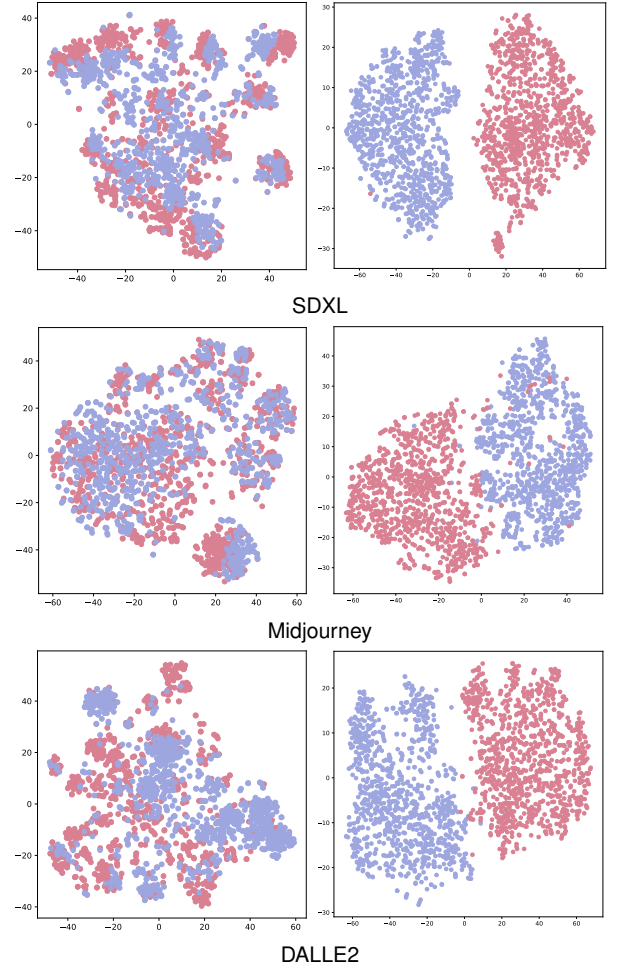


Fig. 3. t-SNE visualization [88] of feature spaces: CLIP [77] (left) versus our EXIF-induced extractor (right), contrasting photographic (red) and AI-generated (blue) images.

where  $\boldsymbol{\omega} = \{\pi_k, \boldsymbol{\mu}_k, \boldsymbol{\Sigma}_k\}_{k=1}^K$ ,  $\pi_k \geq 0$  and  $\sum_k \pi_k = 1$ . Parameters are estimated by maximizing the training log-likelihood via expectation-maximization [90]. Given training features  $\{\mathbf{v}^{(i)}\}_{i=1}^M$ , the E-step computes responsibilities:

$$q_k^{(i)} = \frac{\pi_k \mathcal{N}(\mathbf{v}^{(i)}; \boldsymbol{\mu}_k, \boldsymbol{\Sigma}_k)}{\sum_{k'=1}^K \pi_{k'} \mathcal{N}(\mathbf{v}^{(i)}; \boldsymbol{\mu}_{k'}, \boldsymbol{\Sigma}_{k'})}. \quad (8)$$

With  $M_k = \sum_{i=1}^M q_k^{(i)}$ , the M-step updates are

$$\pi_k = \frac{M_k}{M}, \quad (9)$$



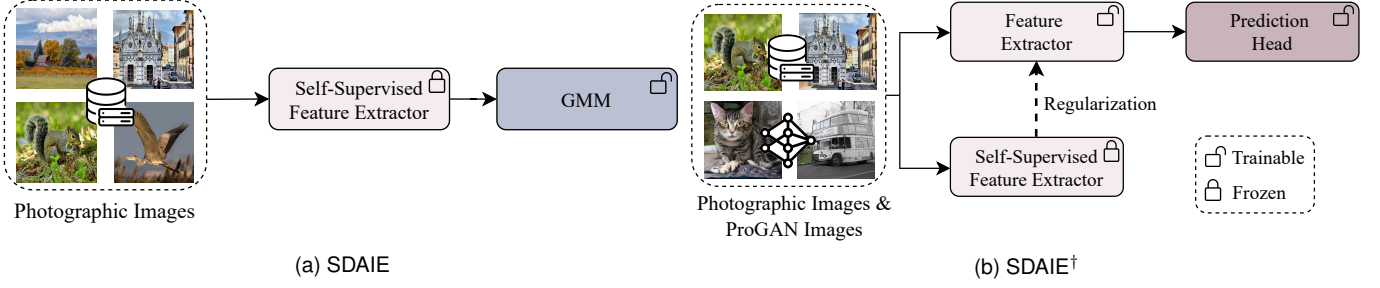


Fig. 4. Overview of SDAIE and SDAIE<sup>†</sup>. **(a)** One-class detection: modeling EXIF-induced photographic features with a GMM. **(b)** Binary detection: regularizing the classifier by the pretext feature extractor to preserve camera-intrinsic cues.

$$\mu_k = \frac{1}{M_k} \sum_{i=1}^M q_k^{(i)} \mathbf{v}^{(i)}, \quad (10)$$

$$\Sigma_k = \frac{1}{M_k} \sum_{i=1}^M q_k^{(i)} (\mathbf{v}^{(i)} - \mu_k)(\mathbf{v}^{(i)} - \mu_k)^\top. \quad (11)$$

At inference, an image is scored by its log-likelihood  $s(\mathbf{v}) = \log p(\mathbf{v}; \omega)$ . Photographic images similar to the training modes receive high scores, whereas AI-generated images tend to have low scores under the learned distribution. We set a decision threshold  $\tau$  to the  $\rho$ -th quantile of training log-likelihoods and predict “AI-generated” whenever  $s(\mathbf{v}) < \tau$ . Generally, we choose a small  $\tau$  to control the false alarm rate on photographic images.

### 3.4 SDAIE<sup>†</sup>

To further improve detection accuracy, we revisit the widely used binary classification paradigm for AI-generated image detection [17], [18], [55]. In this setting, images synthesized by one or more generative models are treated as negative samples, while photographic images serve as positive samples (aligning with SDAIE). However, as discussed in the Introduction, the breadth and rapid evolution of generative models make it unlikely that a supervised detector trained on a finite set of generators can achieve sufficient coverage and robust generalization to unseen models.

To mitigate overfitting to the training generators, we draw on the idea of learning without forgetting [91] and regularize the classifier using the self-supervised feature extractor. Specifically, we cache intermediate and final feature representations of training images computed by the self-supervised extractor, denoted  $\{\{v_l(\mathbf{x}^{(i)}; \theta^*)\}_{l \in \mathcal{L}}\}_{i=1}^M$ , where  $\theta^*$  are the extractor parameters learned via the EXIF-induced self-supervised task, and  $\mathcal{L}$  indexes the stored feature stages. With the original heads removed, the network is equipped with a new prediction head  $g(\cdot; \psi)$ , comprising a fully connected layer followed by a sigmoid. Training jointly optimizes  $\theta$  and  $\psi$  to maximize detection accuracy while retaining EXIF-aligned features. The detection loss is the standard cross-entropy:

$$\ell_{\text{cls}}(\mathbf{x}; \theta, \psi) = -p(\mathbf{x}) \log(g(\mathbf{v}(\mathbf{x}; \theta); \psi)) - (1 - p(\mathbf{x})) \log(1 - g(\mathbf{v}(\mathbf{x}; \theta); \psi)), \quad (12)$$

where  $p(\mathbf{x}) = 1$  for photographic images and  $p(\mathbf{x}) = 0$  otherwise. Feature preservation is enforced by an  $\ell_2$ -induced

matching regularizer that transfers camera-intrinsic knowledge from the pretext feature extractor:

$$\ell_{\text{reg}}(\mathbf{x}; \theta) = \frac{1}{|\mathcal{L}|} \sum_{l \in \mathcal{L}} \frac{1}{D_l} \|\mathbf{v}_l(\mathbf{x}; \theta^*) - \mathbf{v}_l(\mathbf{x}; \theta)\|_2^2, \quad (13)$$

where  $D_l = \dim(\mathbf{v}_l)$  returns the dimension of the (flattened) representation at layer  $l$ . Per-layer normalization by  $D_l$  and average over  $l$  make the penalty scale-invariant across layers. Finally, the minibatch loss combines the two terms:

$$\ell(\mathcal{B}; \theta, \psi) = \frac{1}{|\mathcal{B}|} \sum_{\mathbf{x} \in \mathcal{B}} \left( \ell_{\text{cls}}(\mathbf{x}; \theta, \psi) + \gamma \ell_{\text{reg}}(\mathbf{x}; \theta) \right), \quad (14)$$

where  $\gamma$  controls the trade-off between detection accuracy and feature consistency.

Importantly, EXIF metadata is used only in the self-supervised stage, encouraging EXIF-aligned features beneficial for detecting AI-generated images. In both SDAIE and SDAIE<sup>†</sup> training, as well as at inference, EXIF fields are neither accessed nor required. In other words, predictions rely solely on image pixels. Consequently, any removal, corruption, or manipulation of EXIF metadata at test time has no effect on model performance.

## 4 EXPERIMENTS

In this section, we conduct comprehensive experiments to assess both one-class SDAIE and binary SDAIE<sup>†</sup> detectors. We first describe the experimental setups, including datasets, competing methods, and hyperparameter configurations. We then evaluate detection performance across a wide range of generative models and conclude with ablation studies, isolating the contributions of key components.

### 4.1 Experimental Setups

**Datasets.** We construct our training and evaluation data as follows. For pre-training the EXIF-induced feature extractor, we randomly sample 0.93M photographic images from YFCC100M [100], retaining only samples whose EXIF metadata contains the fourteen tags listed in Table 1. For one-class SDAIE, the GMM is fitted on a mixed set of 10k photographic images drawn from ImageNet [101] and LSUN [102]. For binary SDAIE<sup>†</sup>, we follow established practice [23], [55], [63] and use a 720k training set, comprising 360k LSUN photographs and 360k ProGAN-generated images [6]. For main experiments, we assess

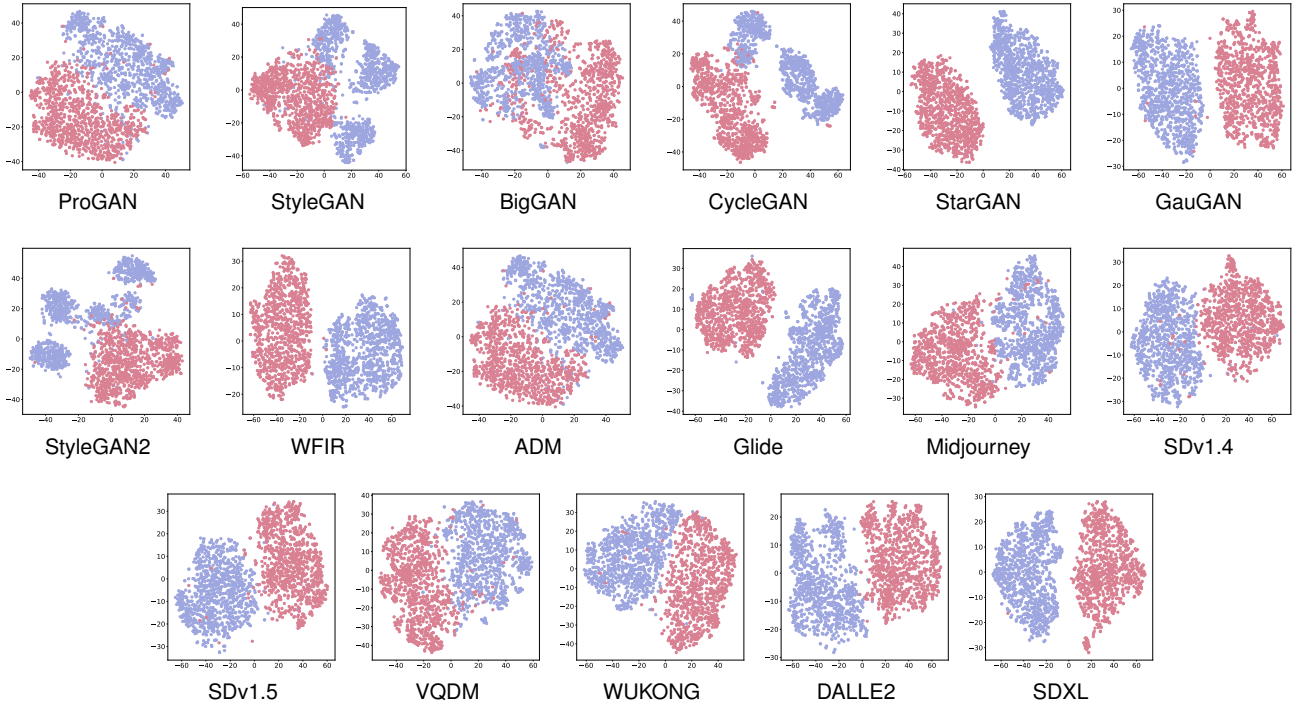


Fig. 5. t-SNE visualization of EXIF-induced features showing a clear separation between photographic (red) and AI-generated (blue) images.

TABLE 2  
Details of evaluation benchmarks.

Generator	Image Size	Image Number	Photographic Source
ProGAN [6]	$256 \times 256$	8.0k	LSUN
StyleGAN [92]	$256 \times 256$	12.0k	LSUN
BigGAN [7]	$256 \times 256$	4.0k	ImageNet
CycleGAN [93]	$256 \times 256$	2.6k	ImageNet
StarGAN [94]	$256 \times 256$	4.0k	CelebA
GauGAN [95]	$256 \times 256$	10.0k	COCO
StyleGAN2 [96]	$256 \times 256$	15.9k	LSUN
WFIR [97]	$1024 \times 1024$	2.0k	FFHQ
ADM [8]	$256 \times 256$	12.0k	ImageNet
Glide [98]	$256 \times 256$	12.0k	ImageNet
Midjourney [28]	$1,024 \times 1,024$	12.0k	ImageNet
SDv1.4 [52]	$512 \times 512$	12.0k	ImageNet
SDv1.5 [52]	$512 \times 512$	16.0k	ImageNet
VQDM [9]	$256 \times 256$	12.0k	ImageNet
WUKONG [99]	$512 \times 512$	12.0k	ImageNet
DALLE2 [53]	$256 \times 256$	2.0k	ImageNet
SDXL [51]	$1,024 \times 1,024$	4.0k	COCO

generalization across seventeen generators: 1) ProGAN [6], 2) StyleGAN [92], 3) BigGAN [7], 4) CycleGAN [93], 5) StarGAN [94], 6) GauGAN [95], 7) StyleGAN2 [96], 8) WFIR [97], 9) ADM [8], 10) Glide [98], 11) Midjourney [28], 12) SDv1.4 [52], 13) SDv1.5 [52], 14) VQDM [9], 15) WUKONG [99], 16) DALLE2 [53], and 17) SDXL [51] (more details in Table 2).

**Competing Methods.** AI-generated image detection spans diverse modeling assumptions and feature biases. To ensure broad and fair coverage, we compare against nine representative detectors selected for methodological diversity (*e.g.*, texture/spectrum cues, local-global fusion, denoiser-based residuals, discriminator-gradient features, diffusion-

oriented reconstruction signals, and semantics-driven embeddings), strong reported performance, and complementary sensitivity to GAN- and diffusion-era artifacts.

- 1) CNNSpot [55] (CVPR’20) adopts a plain ResNet-50 with simple augmentations (*e.g.*, JPEG compression) to improve generalization. Owing to its simplicity and effectiveness, it is widely used as a baseline.
- 2) GramNet [103] (CVPR’20) strengthens texture modeling by inserting Gram operators into a ResNet-like architecture.
- 3) Frank20 [17] (ICML’20) distinguishes photographic from AI-generated images by contrasting their frequency spectra.
- 4) Ju22 [104] (ICIP’22) integrates local and global representations to enhance detection.
- 5) LNP [62] (ECCV’22) exposes AI-generated imagery via noise residuals extracted from a pre-trained denoiser.
- 6) LGrad [63] (CVPR’23) uses gradients of the StyleGAN discriminator with respect to the input image as features, which are classified by a ResNet50.
- 7) DIRE [18] (ICCV’23) targets diffusion-generated images by measuring reconstruction errors along forward and reverse diffusion trajectories.
- 8) UnivFD [23] (CVPR’23) builds on a pre-trained CLIP image encoder to leverage strong semantic representations for visual comprehension and detection.
- 9) NPR [105] (CVPR’24) detects structural artifacts induced by ubiquitous upsampling operators through analysis of neighboring pixel statistics.

For a fair and reproducible comparison, we retrain all competing methods on the same training set using their official code releases. Importantly, we verify our reproduced

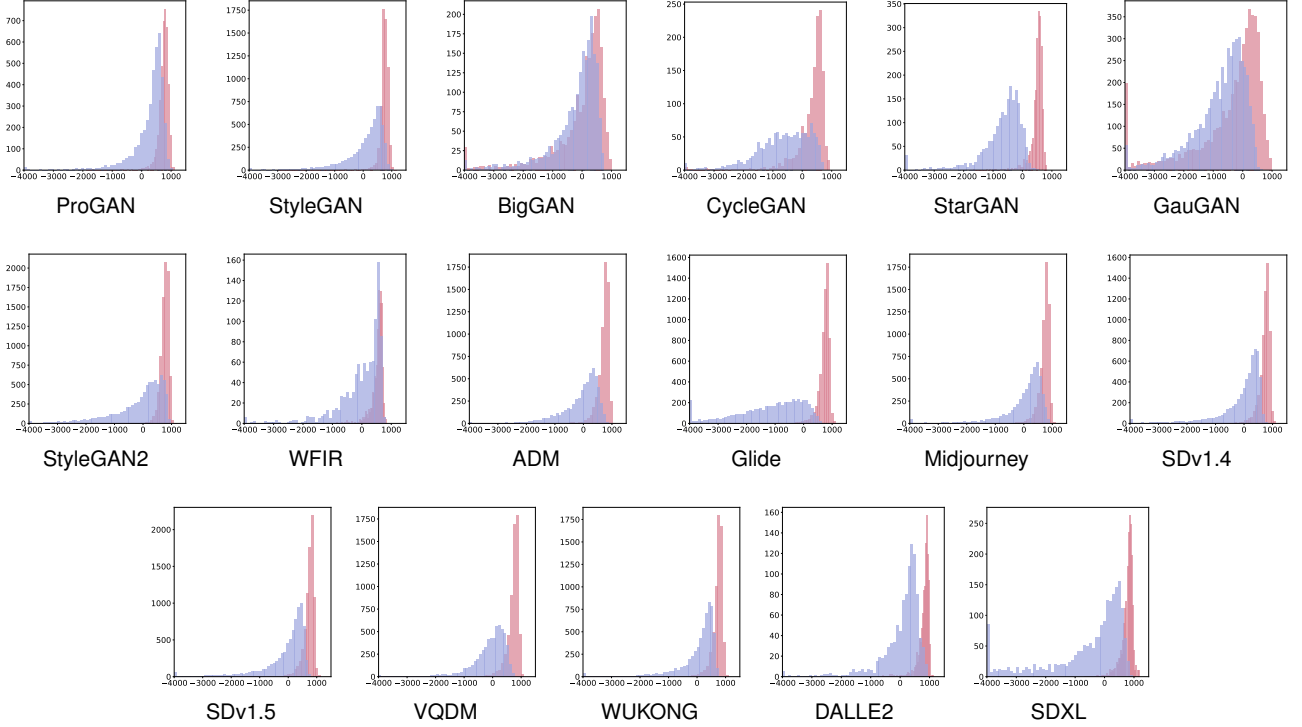


Fig. 6. SDAIE log-likelihood profiles for photographic (red) and AI-generated (blue) images.

results against the numbers reported in the corresponding papers to ensure consistency and reliability.

**Implementation Details.** We learn the EXIF-induced feature extractor exclusively from photographs. For each training image, we extract  $N = 16$  scrambled patches of size  $S = 64$ . The feature extractor uses  $|\mathcal{L}| = 11$  convolution blocks with  $3 \times 3$  kernels, followed by covariance pooling to produce a 528-dim image representation. The trade-off parameters  $\alpha, \beta$  are all set to 1. Optimization is carried out by Adam with a fixed learning rate of  $10^{-4}$ , a minibatch size of 64, and a total of 30,000 iterations.

For one-class SDAIE, we model the distribution of EXIF-induced photographic features with a GMM using  $K = 5$  components. At test time, the detection threshold  $\tau$  is set to the 2-nd quantile of training likelihoods, which corresponds to a training-set false alarm rate below 2%. For binary variant SDAIE<sup>†</sup>, we attach a sigmoid classification head and optimize the sum of the cross-entropy and the representation-alignment regularizer (Eq. (14)). We use Adam with learning rate  $10^{-3}$ , minibatch size 100, and 1,800 iterations; the trade-off weight is  $\gamma = 0.05$ .

To improve generalization [23], [55], we treat common image processing operations as benign perturbations and apply them as data augmentations during training. Specifically, we include

- JPEG compression with the quantization factor sampled from  $\mathcal{U}[90, 100]$ ;
- Bilinear downsampling with the scaling ratio sampled from  $\mathcal{U}[0.25, 1]$ ;
- Gaussian blurring with the standard deviation sampled from  $\mathcal{U}[0, 1]$ .

In the detection phase, we extract all non-overlapping

$64 \times 64$  patches from each test image, and feed them to the learned detectors to screen AI-generated content.

## 4.2 Main Results

We employ two complementary metrics to assess AI-generated image detection performance: 1) detection accuracy (Acc) and 2) mean average precision (mAP).

**One-Class SDAIE Results.** We first conduct a qualitative assessment of SDAIE. Fig. 5 applies t-SNE [88] to the EXIF-induced features, and reveals a clear separation between photographic and AI-generated images. This separation shows that the learned representations effectively capture camera-intrinsic regularities, supporting the feasibility of detecting AI-generated images using self-supervised learning solely on photographic data. Fig. 6 further shows the log-likelihood histograms, where AI-generated images consistently attain lower log-likelihoods than photographic ones in most cases, with only minor distributional overlap. Such behavior is precisely what is desired in a one-class setting, as it allows for reliable discrimination of AI-generated images while maintaining a low false alarm rate.

We next report quantitative results in Tables 3 and 4. The seventeen evaluated generative models are grouped into two categories: GAN-based and diffusion-based generators. Across this diverse collection of models, SDAIE attains non-trivial detection performance despite never observing AI-generated images during training. This outcome underscores the effectiveness of our EXIF-induced self-supervised learning strategy in shaping a feature space where AI-generated images emerge as low-likelihood outliers relative to the distribution of photographic images.



TABLE 3  
Detection performance (Acc/mAP) on GAN-based generators.

Method	ProGAN	StyleGAN	BigGAN	CycleGAN	StarGAN	GauGAN	StyleGAN2	WIFR	Average
CNNSpot	<b>100.0/100.0</b>	90.2/99.8	71.20/86.00	87.6/94.9	94.6/99.0	81.4/90.8	86.9/99.5	<b>91.7/99.9</b>	88.0/96.2
GramNet	<b>100.0/100.0</b>	87.1/99.2	67.30/81.80	86.1/95.3	95.1/99.2	69.4/85.0	87.3/99.1	86.8/95.2	84.9/94.4
Frank20	<b>99.4/100.0</b>	78.0/89.0	82.00/93.60	78.8/84.8	94.6/99.5	80.6/82.8	66.2/82.5	50.8/55.9	78.8/86.0
Ju22	<b>100.0/100.0</b>	85.2/99.5	77.40/90.70	87.0/95.5	97.0/99.8	77.0/88.3	83.3/99.6	66.8/93.3	84.2/95.8
LNP	<b>100.0/100.0</b>	92.6/99.3	88.40/94.50	79.1/89.5	<b>100.0/100.0</b>	79.2/84.5	93.8/99.7	50.0/42.8	85.4/88.8
LGrad	<b>100.0/100.0</b>	90.5/98.9	88.80/96.30	85.7/94.0	99.6/ <b>100.0</b>	82.8/92.9	87.8/92.9	58.2/60.1	86.7/91.9
DIRE-G	95.2/99.1	83.0/91.7	70.10/75.30	74.2/80.6	95.5/99.3	67.8/72.2	75.3/88.3	58.1/60.1	77.4/83.3
DIRE-D	52.8/58.8	51.3/56.7	49.70/46.90	49.6/50.0	46.7/40.6	51.2/47.3	51.7/58.0	53.3/59.0	50.8/52.2
UnivFD	99.8/ <b>100.0</b>	84.9/97.6	<b>95.10/99.30</b>	<b>98.3/99.8</b>	95.8/99.4	<b>99.5/100.0</b>	75.0/97.9	86.9/96.7	91.9/ <b>98.8</b>
NPR	99.9/ <b>100.0</b>	96.1/99.9	87.30/94.00	90.3/99.1	99.6/ <b>100.0</b>	85.4/88.7	98.1/ <b>100.0</b>	60.7/94.0	89.7/97.0
SDAIE	78.6/87.3	84.8/89.7	57.90/66.00	66.2/85.9	74.5/99.1	55.3/73.4	85.0/89.5	71.5/79.4	71.7/83.8
SDAIE <sup>†</sup>	<b>100.0/100.0</b>	<b>99.8/100.0</b>	90.50/97.30	91.9/99.4	<b>100.0/100.0</b>	84.0/89.9	<b>99.2/100.0</b>	84.5/98.1	<b>93.7/98.1</b>

TABLE 4  
Detection performance (Acc/mAP) on diffusion-based generators.

Method	ADM	Glide	Midjourney	SDv1.4	SDv1.5	VQDM	WUKONG	DALLE2	SDXL	Average
CNNSpot	60.4/75.7	58.1/72.3	51.4/66.2	50.6/61.2	50.5/61.6	56.5/68.8	51.0/57.3	50.5/53.5	53.0/72.6	53.6/65.5
GramNet	58.6/73.1	54.5/66.8	50.0/56.8	51.7/59.8	52.2/60.4	52.9/61.1	50.8/55.6	49.3/49.8	64.5/68.2	53.8/61.3
Frank20	63.4/61.8	54.1/52.9	45.9/46.1	38.8/37.8	39.2/37.8	77.8/85.1	40.3/39.6	34.7/38.2	51.2/49.5	49.5/49.9
Ju22	49.0/94.1	57.2/77.5	52.2/70.0	51.0/65.4	51.4/65.7	55.1/75.6	51.7/64.6	52.8/68.1	55.6/79.4	52.9/73.4
LNP	83.9/93.4	83.5/92.8	69.6/86.9	89.3/96.3	88.8/96.0	85.0/94.9	86.4/95.3	92.5/98.3	87.8/87.8	85.2/93.5
LGrad	66.2/73.5	71.7/84.4	70.5/77.7	65.2/68.9	65.9/69.3	74.7/79.5	60.3/65.7	71.3/86.4	71.3/80.0	68.6/76.2
DIRE-G	75.8/85.8	71.8/78.4	58.0/61.9	49.7/49.9	49.8/49.5	53.7/54.6	54.5/55.4	66.5/74.5	55.4/54.0	59.5/62.7
DIRE-D	<b>98.3/99.8</b>	92.4/99.5	89.5/97.3	91.2/98.6	91.6/98.8	<b>91.9/99.0</b>	90.9/98.4	92.5/99.7	91.3/99.1	92.2/98.9
UnivFD	66.9/86.8	62.5/83.8	56.1/74.0	63.7/86.1	63.5/85.8	85.3/96.5	70.9/91.1	50.8/63.0	50.7/67.6	63.4/81.6
NPR	84.9/98.3	<b>96.7/99.6</b>	92.6/99.0	<b>97.4/99.7</b>	<b>97.5/99.6</b>	90.1/ <b>99.2</b>	91.7/98.9	<b>99.6/100.0</b>	<b>98.6/99.6</b>	<b>94.3/99.3</b>
SDAIE	88.9/95.9	93.2/99.3	85.6/92.8	89.7/96.5	89.7/96.4	90.8/97.2	87.5/95.6	89.0/95.9	89.4/96.6	89.3/96.2
SDAIE <sup>†</sup>	92.9/98.3	93.1/98.5	<b>95.4/99.4</b>	95.8/ <b>99.9</b>	95.7/ <b>99.8</b>	91.5/97.9	<b>95.0/99.4</b>	97.1/99.9	96.6/ <b>100.0</b>	<b>94.8/99.2</b>

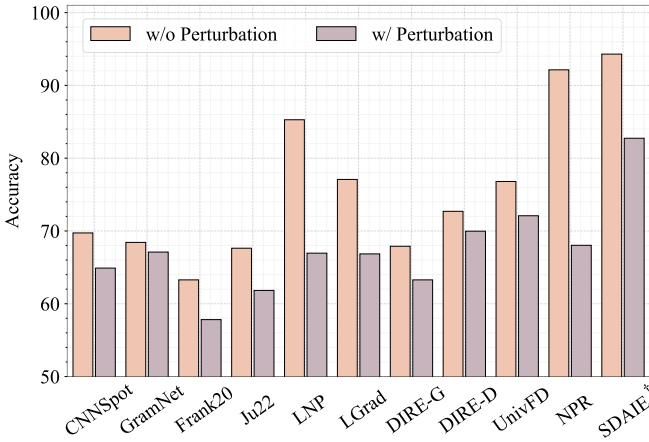


Fig. 7. Overall robustness of AI-generated image detectors under benign post-processing perturbations.

Interestingly, SDAIE attains noticeably higher mean detection performance on diffusion-based generators than on GAN-based ones. This may arise because EXIF-induced representations are explicitly aligned with camera-intrinsic residual statistics. Diffusion models synthesize images via iterative denoising, without modeling the physical imaging pipeline, and consequently fail to reproduce sensor noise, demosaicing periodicity, and compression fingerprints captured by SDAIE. By contrast, several of the GAN-based

benchmarks operate on narrow, constrained photographic domains and can partially mimic camera-like residuals, leading to greater overlap with the photographic manifold and slightly reduced one-class separability.

**Binary SDAIE<sup>†</sup> Results.** We next evaluate the binary variant SDAIE<sup>†</sup>, which is regularized by the EXIF-induced feature extractor. Tables 3 and 4 show that SDAIE<sup>†</sup> surpasses most competing methods by a clear margin across both GAN-based and diffusion-based generators. All competing detectors, except DIRE-D, are trained on a mixture of photographic and ProGAN-generated images, yet most degrade substantially when evaluated on diffusion-based content, whereas SDAIE<sup>†</sup> maintains strong accuracy in this setting. We attribute this superior cross-model generalization to the core design of SDAIE<sup>†</sup>, which detects AI-generated images by leveraging EXIF-induced representations intrinsic to photographic images rather than artifacts tied to specific generative models. Consequently, even when ProGAN is the only synthetic source during training, SDAIE<sup>†</sup> remains effective on diffusion-generated images.

In contrast, conventional methods are explicitly designed and optimized to capture “universal” generative artifacts, whose discriminative power inevitably diminishes as generation architectures and synthesis pipelines evolve. DIRE-D, which is trained on diffusion-based synthetic data, exemplifies this limitation: it achieves competitive detection performance on diffusion-generated images but suffers pronounced accuracy degradation on GAN-generated images

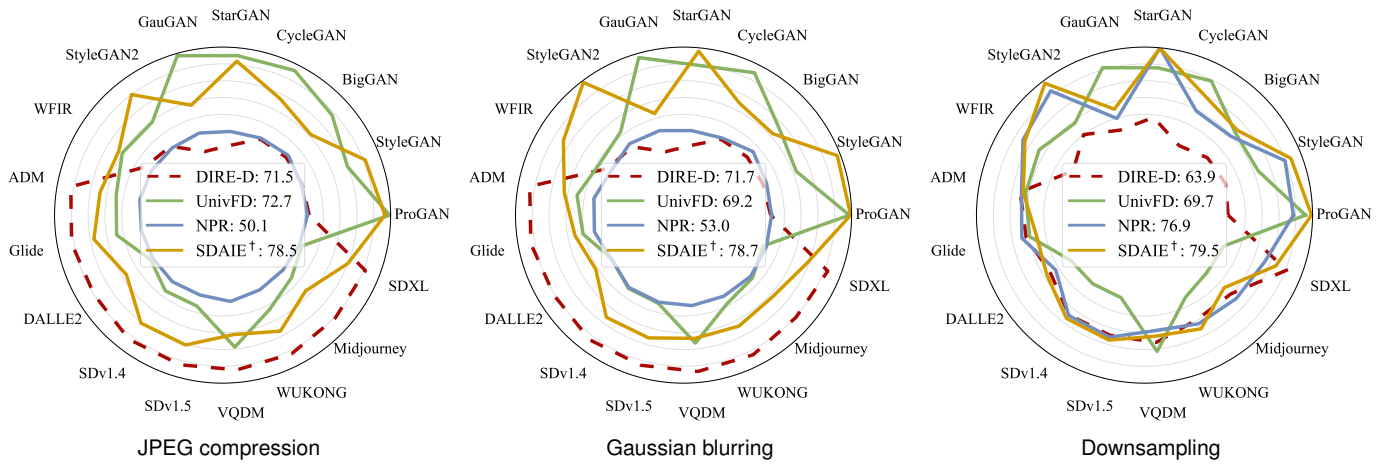


Fig. 8. Robustness of AI-generated image detectors to individual benign post-processing operators. The legend represents the average detection accuracy of each detector.

due to mismatch in artifact characteristics. Among the remaining, UnivFD is the closest competitor to SDAIE<sup>†</sup> on GAN-based generators. Yet, its semantics-oriented detection principle leads to strong performance mainly where GAN-generated images exhibit more conspicuous semantic or structural anomalies, and to weaker performance on diffusion-based generators whose outputs are often semantically coherent and visually refined. Compared with another state-of-the-art method, NPR [62], SDAIE<sup>†</sup> achieves higher accuracy, especially on GAN-based generators. NPR identifies AI-generated images via artifacts introduced by upsampling layers, and its generalization relies on the ubiquity and stability of such operators in image generation. However, as modern generators increasingly adopt architectures with reduced or carefully compensated upsampling, these artifact cues become unreliable or even absent in practice. In addition, camera pipelines may introduce aliasing and interpolation effects that resemble synthetic upsampling, leading to inflated false negatives.

**Robustness to Benign Perturbations.** In real-world deployments, AI-generated images are seldom encountered in their pristine form; instead, they typically undergo routine post-processing operations such as JPEG compression, mild blurring, or rescaling along acquisition, transmission, and display pipelines. These label-preserving transformations may weaken or even obscure forensic cues, thereby challenging the robustness of detectors. To systematically assess this aspect, we subject all detectors to three commonly used operators: JPEG compression with a quality factor of 95, Gaussian blurring with a standard deviation of 1, and downsampling by a factor of 2 along both spatial dimensions. Fig. 7 summarizes the overall robustness by reporting, for each detector, the mean detection accuracy across seventeen generators. While several competing methods, especially NPR, perform strongly on pristine images, their mean accuracies drop substantially when benign perturbations are introduced. In contrast, SDAIE<sup>†</sup> maintains high accuracy across all scenarios and achieves the best aggregated performance, suggesting that the EXIF-induced, camera-intrinsic representations affords a more stable basis

for AI-generated image detection.

Fig. 8 provides a more fine-grained view of the robustness of SDAIE<sup>†</sup> against three strong competitors—DIRE-D, UnivFD, and NPR—by breaking down performance according to the specific post-processing operator. Generally, JPEG compression and Gaussian blurring emerge as the most challenging perturbations: both aggressively attenuate high-frequency components where many synthesis-related cues (e.g., periodic artifacts and subtle noise inconsistencies) reside. In contrast, 2× downsampling tends to be comparatively less destructive, since it primarily reduces spatial resolution while still preserving a portion of the global structural and color statistics that remain informative for detection. SDAIE<sup>†</sup> preserves its advantage under all three operators, showing the smallest relative degradation when strong high-frequency suppression is applied. This operator-wise analysis reveals that robustness to frequency-suppressing transformations is the key bottleneck for current detectors, and that the EXIF-induced, camera-intrinsic features offer a more resilient solution in this regime.

**Generalization to Emerging Generators and In-the-Wild Images.** Beyond the curated benchmark suite, we further assess whether SDAIE<sup>†</sup> can keep pace with rapidly evolving generative models and in-the-wild content circulating on social media. To this end, we collect additional AI-generated images using four recent text-to-image models: FLUX.1 [106], FLUX.1-Kontext [106], SD-3.5-Turbo [107], and Qwen-Image [108], all conditioned on captions from the COCO dataset [109]. We produce 1,000 images per model. In parallel, we collect in-the-wild AI-generated images attributed to Midjourney [28] (latest v7 release), Tongyi [110], and Lummi [111], each comprising 1,000 images, from public social platforms. These images better reflect realistic use cases with prompt, style, and post-processing diversities.

Table 5 compares SDAIE<sup>†</sup> against UnivFD and NPR in terms of detection accuracy. It is clear that SDAIE<sup>†</sup> consistently attains the highest performance across all generators, which exhibits substantial visual and stylistic variability. NPR also maintains relatively strong accuracy on most sources, but trails SDAIE<sup>†</sup> by 4–24 percentage points, par-

TABLE 5  
Generalization (Acc) of AI-generated image detectors to emerging generators and in-the-wild images.

Method	FLUX.1	FLUX.1-Kontext	SD-3.5-Turbo	Qwen-Image	Midjourney	Tongyi	Lummi	Average
UnivFD	0.1	0.8	2.2	6.5	2.8	0.9	4.5	2.5
NPR	90.0	90.0	89.8	70.0	98.8	81.1	69.9	84.2
SDAIE <sup>†</sup>	<b>96.2</b>	<b>96.6</b>	<b>94.8</b>	<b>94.1</b>	<b>99.0</b>	<b>98.1</b>	<b>84.7</b>	<b>94.8</b>

TABLE 6  
Choice of feature extractor on detection performance (Acc/mAP).

Generator	CLIP	EAL	SDAIE
ProGAN	76.21/82.85	50.15/51.27	<b>78.59/87.25</b>
StyleGAN	51.99/50.18	48.61/68.26	<b>84.84/89.73</b>
BigGAN	<b>71.03/73.71</b>	33.80/38.20	57.85/66.01
CycleGAN	<b>78.84/89.65</b>	57.08/70.79	66.24/85.88
StarGAN	50.08/98.87	44.62/31.76	<b>74.49/99.13</b>
GauGAN	<b>63.12/70.25</b>	41.06/39.05	55.33/73.43
StyleGAN2	37.07/43.36	46.35/55.28	<b>85.02/89.51</b>
WFIR	53.20/60.12	47.00/50.53	<b>71.45/79.38</b>
ADM	48.08/57.45	72.90/93.87	<b>88.85/95.91</b>
Glide	46.50/53.87	<b>93.25/97.96</b>	93.24/99.33
Midjourney	49.39/54.16	59.06/75.26	<b>85.58/92.83</b>
SDv1.4	45.18/45.39	51.93/80.97	<b>89.72/96.46</b>
SDv1.5	45.37/45.53	52.74/81.61	<b>89.65/96.44</b>
VQDM	45.58/53.47	67.06/91.94	<b>90.76/97.19</b>
WUKONG	49.33/48.94	53.87/81.63	<b>87.49/95.59</b>
DALLE2	42.90/45.50	76.25/99.00	<b>88.95/95.94</b>
SDXL	51.85/53.99	53.35/82.45	<b>89.35/96.59</b>
Average	53.28/60.43	55.83/69.99	<b>81.02/90.39</b>

ticularly on Qwen-Image and Tongyi. In contrast, UnivFD almost completely fails in this regime, underscoring the limitations of semantics-oriented CLIP features once emerging generators achieve high semantic plausibility and stylistic diversity. Taken together with the benchmark results, these findings indicate that EXIF-induced, camera-intrinsic representations provide a robust and forward-compatible basis for detecting AI-generated images: they transfer reliably to unseen architectures, remain effective on real-world social media content, and avoid overfitting to artifacts specific to any particular generation family or deployment pipeline.

**Evaluation on Other Image Formats.** Because our detection pipeline is trained exclusively on photographic and AI-generated images, it is interesting to see its behavior on semantic formats that lie clearly outside this training distribution. Specifically, we collect 1,000 hand-drawn or computer-aided cartoon images [112] and use them as an out-of-distribution test set. SDAIE<sup>†</sup> identifies 98.7% of these images as non-AI-generated, closely matching UnivFD and NPR (99.5% and 97.4%, respectively). The results therefore demonstrate that SDAIE<sup>†</sup>, like existing methods, behaves conservatively on such out-of-distribution content, assigning it to the non-AI-generated side of the binary decision rather than over-claiming AI attribution.

### 4.3 Ablation Studies

We conduct a series of ablation studies to disentangle the contributions of the pretext task, network architecture, EXIF-induced regularization, and data augmentation to the overall performance of SDAIE and SDAIE<sup>†</sup>.

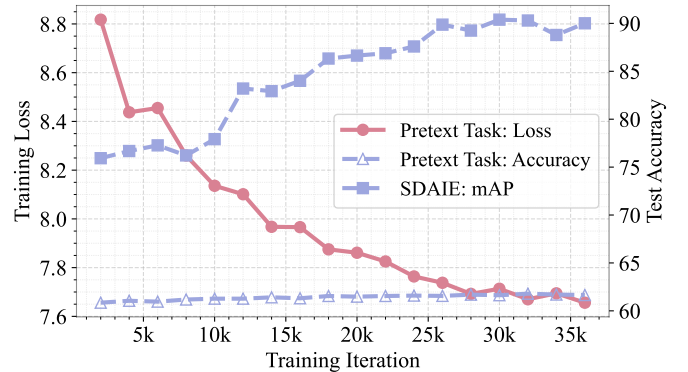


Fig. 9. Effect of EXIF prediction accuracy on one-class detection performance of SDAIE.

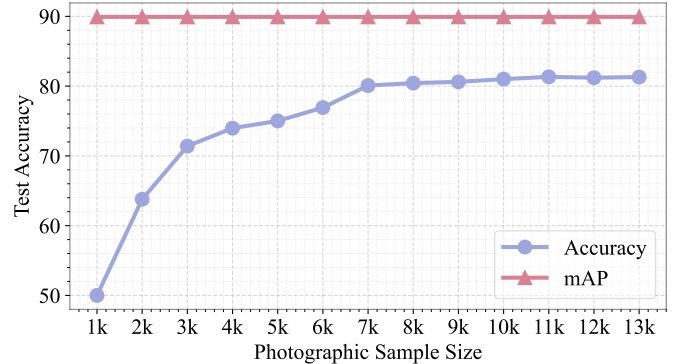


Fig. 10. Effect of photographic training sample size on SDAIE.

**Choice of Feature Extractor.** To demonstrate the importance of the EXIF-induced pretext task, we compare SDAIE with two alternative feature extractors trained on different pretext objectives: (1) the image encoder of CLIP, trained on large-scale image-text pairs, and (2) EAL [24], trained on image-EXIF pairs. For all three extractors, one-class detection is implemented via a GMM in feature space.

Table 6 shows that, averaged across all seventeen generators, SDAIE clearly outperforms both CLIP and EAL. CLIP’s performance deteriorates when AI-generated images become semantically plausible and diverse, reflecting its reliance on high-level semantics. EAL, while EXIF-aware, still lags behind SDAIE. We conjecture that learning from textual EXIF descriptions makes it difficult to capture fine-grained numerical relationships (*e.g.*, between ISO 100 and ISO 400) embedded in long, information-dense text, whereas our direct classification and ranking over tag values offer a more precise way to encode camera-specific statistics.

**Impact of EXIF Prediction Accuracy on SDAIE.** We first

TABLE 7

Effect of network components and patch size on detection performance (Acc/mAP) of SDAIE and SDAIE<sup>†</sup>.

Configuration	SDAIE	SDAIE <sup>†</sup>
w/o Patch Scrambling	80.56/88.25	80.02/87.72
w/o High-Pass Filtering	66.84/77.90	81.17/89.19
w/o Covariance Pooling	78.21/87.73	89.14/95.04
All (w/ Patch Size of $16 \times 16$ )	78.93/ <b>92.63</b>	84.09/90.16
All (w/ Patch Size of $64 \times 64$ )	<b>81.02/90.39</b>	<b>94.30/98.69</b>

examine how the quality of the EXIF-induced pretext task influences one-class detection. Fig. 9 plots the evolution of the pretext training loss and test accuracy, together with the mAP of SDAIE, as a function of training iterations. As the cross-entropy loss of the pretext task decreases, its prediction accuracy improves, and the mAP of SDAIE also increases. Both curves gradually plateau once the number of iterations exceeds roughly 28,000, showing that further optimizing the pretext task yields diminishing returns for downstream detection. This positive correlation confirms that better EXIF prediction directly translates into a more discriminative photographic feature space for one-class AI-generated image detection.

**Effect of Photographic Sample Size on SDAIE.** SDAIE models the distribution of EXIF-induced features using a GMM fitted on a set of photographic images. We therefore study how its performance varies with the number of available photographic samples. Fig. 10 reports the mean results across seventeen generators as we vary the number of training photographs from 1,000 to 10,000.

Even with only 1,000 photographs, SDAIE attains an mAP of around 90%, indicating that the EXIF-induced feature extractor already creates a feature space where photographic and AI-generated images are largely separable. As the number of photographs increases, detection performance steadily improves; the average detection accuracy stabilizes around 80% once more than 8,000 images are used. Note that with very few training photographs, estimating a reliable likelihood threshold becomes challenging, and the resulting decision boundary can be unstable.

**Pretext Task Design.** We next assess the design choices in the EXIF-induced pretext task, focusing on how to handle continuous tags. We consider two alternatives: direct regression guided by the mean squared error versus the proposed pairwise ranking. From our experiments, replacing regression with pairwise ranking yields consistent gains. For SDAIE, the accuracy improves from 79.55% to 81.02%. For SDAIE<sup>†</sup>, the gains are even larger, with accuracy rising from 91.38% to 94.30%. These results suggest that modeling relative ordering is more robust to the uneven quantization and noise typical of EXIF numerics than absolute regression, and better aligns the learned representations with camera-intrinsic trends.

**Network Architecture Design.** We then dissect the network architecture, which consists of scrambled patches, a bank of high-pass filters, a convolution encoder with covariance pooling, and a Transformer encoder. Table 7 summarizes the effect of four key design choices: patch scrambling, high-

TABLE 8

Effect of high-pass filter design (see Fig. 2) on detection performance (Acc/mAP) of SDAIE and SDAIE<sup>†</sup>.

Filter	SDAIE	SDAIE <sup>†</sup>
Gabor Filters	76.73/88.01	88.34/96.07
Only (a)	70.01/82.23	83.32/91.83
(a) to (b)	71.43/83.98	84.77/93.70
(a) to (c)	73.76/85.70	87.10/95.33
(a) to (d)	76.89/87.87	89.98/96.56
(a) to (e)	79.50/89.03	91.43/97.39
(a) to (f)	79.39/89.11	91.33/97.31
All ((a) to (g))	<b>81.02/90.39</b>	<b>94.30/98.69</b>

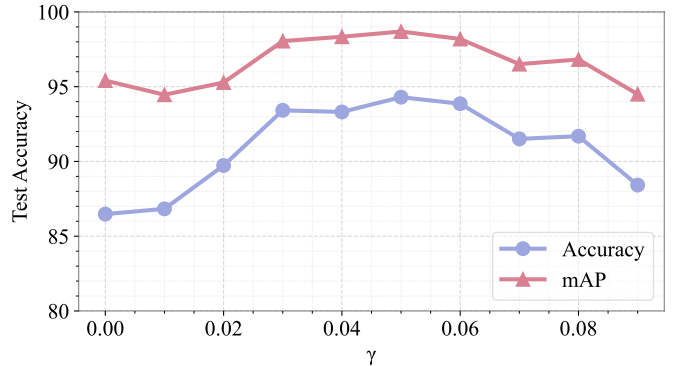


Fig. 11. Effect of EXIF-induced regularization strength on SDAIE<sup>†</sup>.

pass filtering, covariance pooling, and patch size.

When all three modules are enabled with a patch size of  $64 \times 64$ , SDAIE and SDAIE<sup>†</sup> achieve the best performance. Reducing the patch size to  $16 \times 16$  significantly degrades SDAIE<sup>†</sup>, suggesting that very small patches fail to preserve sufficient spatial structure for reliably capturing camera-intrinsic residual patterns. Removing patch scrambling (by adding positional encoding [113]), high-pass filtering, or covariance pooling (replaced with average pooling) each leads to noticeable drops in both accuracy and mAP, confirming that these components are complementary rather than redundant.

**Detailed Impact of High-Pass Filters.** Because high-pass filtering is important to our design, we further analyze its effect in isolation. Our high-pass filter bank comprises 30 filters derived from seven prototype kernels (see Fig. 2). Table 8 reports detection performance as we progressively add filter groups. Both SDAIE and SDAIE<sup>†</sup> benefit monotonically from increasing the number of filters, with the full bank achieving the highest results. This trend suggests that a diverse set of structural and directional filters is essential for exposing subtle residual patterns left by camera pipelines versus synthesis processes.

We also compare our high-pass filtering scheme against Gabor filters [114]. The latter yields inferior performance, confirming that the classical forensic filters of Fridrich and Kodovský [26] are better suited to modeling camera-intrinsic traces in high-frequency residuals than generic orientation-frequency decompositions.

**Effect of the EXIF-induced Regularizer on SDAIE<sup>†</sup>.** In the binary SDAIE<sup>†</sup>, the EXIF-induced feature extractor serves



TABLE 9  
Effect of data augmentation on the accuracy–robustness trade-off for NPR and SDAIE<sup>†</sup> (Acc/mAP).

Data Augmentation	Clean		JPEG Compression		Gaussian Blurring		Downsampling	
	NPR	SDAIE <sup>†</sup>	NPR	SDAIE <sup>†</sup>	NPR	SDAIE <sup>†</sup>	NPR	SDAIE <sup>†</sup>
✗	92.14/98.21	76.48/88.71	50.09/49.06	49.97/49.72	52.96/53.31	60.10/69.89	76.91/80.62	59.83/62.19
✓	87.54/95.36	94.30/98.69	72.85/77.12	78.47/84.38	73.49/77.62	76.68/87.01	70.30/79.40	79.52/86.70

as a regularizer that encourages the detector to preserve camera-intrinsic representations while learning to discriminate between photographs and ProGAN-generated images. The strength of this guidance is governed by  $\gamma$  in Eq. (14).

Fig. 11 shows detection performance for different  $\gamma$ . When  $\gamma = 0$  (*i.e.*, random initialization with no regularization), the accuracy decreases by roughly 8% compared with the best setting, confirming that naively training a binary classifier on ProGAN-generated images versus photographs tends to overfit to generator-specific cues. As  $\gamma$  increases, both accuracy and mAP improve, reaching their peak around  $\gamma = 0.05$ . Further increasing  $\gamma$  beyond 0.7 constrains the classifier too heavily to the pretext representations, leaving insufficient flexibility to adapt to the binary detection task and causing performance to drop.

We also consider a fine-tuning baseline in which a classification head is appended directly to the self-supervised EXIF-induced feature extractor and the entire model is jointly optimized. This strategy achieves an accuracy of 91.78%, which remains notably below the best performance of SDAIE<sup>†</sup> (94.30%). These results emphasize that explicit representation alignment through regularization yields a better trade-off between preserving camera-intrinsic cues and adapting to the supervised detection objective than simple end-to-end fine-tuning.

**Effect of Data Augmentation.** We finally analyze how data augmentation affects the balance between accuracy and robustness for NPR and SDAIE<sup>†</sup> under three benign perturbations: JPEG compression, Gaussian blurring, and downsampling (see Table 9). For SDAIE<sup>†</sup>, augmentation yields consistent gains across both clean and perturbed settings. This signifies that EXIF-induced features can simultaneously benefit from augmentation in terms of generalization to unseen clean images and robustness to post-processed images, without incurring a noticeable trade-off.

For NPR, the effect of augmentation is more delicate and highlights an explicit accuracy–robustness trade-off. Without augmentation, NPR attains high accuracy and mAP on clean inputs, but is extremely fragile to JPEG compression and Gaussian blurring. Introducing the same augmentations substantially improves robustness to such perturbations, but these gains come at the cost of reduced performance on clean and downsampled images. In other words, for NPR, augmentation shifts the decision boundary toward invariance to post-processing, but simultaneously weakens its strong bias toward upsampling-induced local correlation patterns that drive its excellent clean-image performance.

## 5 CONCLUSION AND DISCUSSION

We have described a self-supervised feature extractor that leverages photographic EXIF metadata to guide the learn-

ing of camera-intrinsic representations. The pre-trained extractor maps spatial images into a compact feature space in which photographs and AI-generated images are well separated. Extensive experiments on both one-class and binary detection settings show that our EXIF-induced detectors achieve consistently superior generalization to unseen generators and improved robustness to common post-processing operations.

Despite these promising results, several important questions remain open. First, the current pretext task is designed to predict EXIF-related properties and is therefore only implicitly aligned with the downstream detection objective. A more explicit, automated alignment between pretext and detection tasks [115] may further improve the transferability of the learned representations.

Second, aligning with previous studies [63], [105], our feature extractor and downstream detectors still exhibit a notable reliance on high-frequency traces, which can be fragile under common post-processing operations. Future work should therefore investigate architectures, regularization schemes, and data augmentation strategies that promote a more balanced use of multi-level, multi-scale cues, reducing dependence on high-frequency patterns while preserving sensitivity to subtle generative footprints.

Third, we have considered a one-class detection setting in which any image deviating from the modeled photographic distribution is treated as anomalous (*i.e.*, AI-generated). While this provides a simple mechanism to flag non-photographic content, it remains a coarse approximation of real-world usage. In practice, many non-photographic yet non-AI-generated images (*e.g.*, graphics, paintings, or heavily edited content) are better handled as a distinct category rather than being lumped together with AI-generated imagery. Extending our framework to a more realistic out-of-distribution setting, with a third class explicitly modeling such non-photographic and non-AI-generated images, would better reflect real deployment conditions and help avoid overconfident predictions on genuinely out-of-domain inputs.

Finally, our evaluation inherits the common practice [18], [23], [62], [63], [104], [105] summarized in Table 2, where different generators are tested on heterogeneous photographic datasets. To enable more standardized and comparable benchmarking, an important community effort is to construct and adopt a large-scale, universal set of photographic images shared across generators and detection methods. Doing so would support more rigorous cross-generator comparisons and yield a clearer view of the strengths and limitations of competing detectors.



## REFERENCES

- [1] D. P. Kingma, T. Salimans, R. Jozefowicz, X. Chen, I. Sutskever, and M. Welling, "Improved variational inference with inverse autoregressive flow," in *Advances in Neural Information Processing Systems*, 2016, pp. 4743–4751.
- [2] A. Van den Oord, N. Kalchbrenner, L. Espeholt, O. Vinyals, A. Graves, and K. Kavukcuoglu, "Conditional image generation with PixelCNN decoders," in *Advances in Neural Information Processing Systems*, 2016, pp. 4797–4805.
- [3] D. P. Kingma and M. Welling, "Auto-encoding variational Bayes," *arXiv preprint arXiv:1312.6114*, 2013.
- [4] D. P. Kingma and P. Dhariwal, "Glow: Generative flow with invertible 1x1 convolutions," in *Advances in Neural Information Processing Systems*, 2018, pp. 10215–10224.
- [5] I. Goodfellow, J. Pouget-Abadie, M. Mirza, B. Xu, D. Warde-Farley, S. Ozair, A. Courville, and Y. Bengio, "Generative adversarial nets," in *Advances in Neural Information Processing Systems*, 2014, pp. 2672–2680.
- [6] T. Karras, T. Aila, S. Laine, and J. Lehtinen, "Progressive growing of GANs for improved quality, stability, and variation," in *International Conference on Learning Representations*, 2018, pp. 1–26.
- [7] A. Brock, J. Donahue, and K. Simonyan, "Large scale GAN training for high fidelity natural image synthesis," in *International Conference on Learning Representations*, 2019, pp. 1–35.
- [8] P. Dhariwal and A. Nichol, "Diffusion models beat GANs on image synthesis," in *Advances in Neural Information Processing Systems*, 2021, pp. 8780–8794.
- [9] S. Gu, D. Chen, J. Bao, F. Wen, B. Zhang, D. Chen, L. Yuan, and B. Guo, "Vector quantized diffusion model for text-to-image synthesis," in *IEEE/CVF Conference on Computer Vision and Pattern Recognition*, 2022, pp. 10696–10706.
- [10] J. Ho, A. Jain, and P. Abbeel, "Denoising diffusion probabilistic models," in *Advances in Neural Information Processing Systems*, 2020, pp. 6840–6851.
- [11] V. Karasavva and A. Noorbhai, "The real threat of deepfake pornography: A review of canadian policy," *Cyberpsychology, Behavior, and Social Networking*, vol. 24, no. 3, pp. 203–209, 2021.
- [12] A. de Rancourt-Raymond and N. Smaili, "The unethical use of deepfakes," *Journal of Financial Crime*, vol. 30, no. 4, pp. 1066–1077, 2023.
- [13] D. O'Sullivan and J. Passantino, "'Verified' Twitter accounts share fake image of 'explosion' near Pentagon, causing confusion," <https://www.cnn.com/2023/05/22/tech/twitter-fake-image-pentagon-explosion/index.html>, accessed: Mar 26, 2025.
- [14] N. Carlini, J. Hayes, M. Nasr, M. Jagielski, V. Shwag, F. Tramèr, B. Balle, D. Ippolito, and E. Wallace, "Extracting training data from diffusion models," in *USENIX Security Symposium*, 2023, pp. 5253–5270.
- [15] Z. Kadkhodaie, F. Guth, E. P. Simoncelli, and S. Mallat, "Generalization in diffusion models arises from geometry-adaptive harmonic representations," in *International Conference on Learning Representations*, 2024, pp. 1–25.
- [16] M. Barni, K. Kallas, E. Nowroozi, and B. Tondi, "CNN detection of GAN-generated face images based on cross-band co-occurrences analysis," in *International Workshop on Information Forensics and Security*, 2020, pp. 1–6.
- [17] J. Frank, T. Eisenhofer, L. Schönherr, A. Fischer, D. Kolossa, and T. Holz, "Leveraging frequency analysis for deep fake image recognition," in *International Conference on Machine Learning*, 2020, pp. 3247–3258.
- [18] Z. Wang, J. Bao, W. Zhou, W. Wang, H. Hu, H. Chen, and H. Li, "DIRE for diffusion-generated image detection," in *International Conference on Computer Vision*, 2023, pp. 22445–22455.
- [19] G. Cazenavette, A. Sud, T. Leung, and B. Usman, "FakeInversion: Learning to detect images from unseen text-to-image models by inverting stable diffusion," in *IEEE/CVF Conference on Computer Vision and Pattern Recognition*, 2024, pp. 10759–10769.
- [20] M. Huh, A. Liu, A. Owens, and A. A. Efros, "Fighting fake news: Image splice detection via learned self-consistency," in *European Conference on Computer Vision*, 2018, pp. 101–117.
- [21] V. Chandola, A. Banerjee, and V. Kumar, "Anomaly detection: A survey," *ACM Computing Surveys*, vol. 41, no. 3, pp. 1–58, 2009.
- [22] R. Chalapathy and S. Chawla, "Deep learning for anomaly detection: A survey," *arXiv preprint arXiv:1901.03407*, 2019.
- [23] U. Ojha, Y. Li, and Y. J. Lee, "Towards universal fake image detectors that generalize across generative models," in *IEEE/CVF Conference on Computer Vision and Pattern Recognition*, 2023, pp. 24480–24489.
- [24] C. Zheng, A. Shrivastava, and A. Owens, "EXIF as language: Learning cross-modal associations between images and camera metadata," in *IEEE/CVF Conference on Computer Vision and Pattern Recognition*, 2023, pp. 6945–6956.
- [25] M.-F. Tsai, T.-Y. Liu, T. Qin, H.-H. Chen, and W.-Y. Ma, "FRank: A ranking method with fidelity loss," in *International Conference on Research and Development in Information Retrieval*, 2007, pp. 383–390.
- [26] J. Fridrich and J. Kodovský, "Rich models for steganalysis of digital images," *IEEE Transactions on Information Forensics and Security*, vol. 7, no. 3, pp. 868–882, 2012.
- [27] Z. Li and D. Hoiem, "Learning without forgetting," *IEEE Transactions on Pattern Analysis and Machine Intelligence*, vol. 40, no. 12, pp. 2935–2947, 2017.
- [28] "Midjourney," <https://www.midjourney.com/home/>, accessed: Mar 26, 2025.
- [29] A. Hyvärinen and P. Dayan, "Estimation of non-normalized statistical models by score matching," *Journal of Machine Learning Research*, vol. 6, no. 4, pp. 695–709, 2005.
- [30] M. Arjovsky, S. Chintala, and L. Bottou, "Wasserstein generative adversarial networks," in *International Conference on Machine Learning*, 2017, pp. 214–223.
- [31] T. Salimans, I. Goodfellow, W. Zaremba, V. Cheung, A. Radford, and X. Chen, "Improved techniques for training GANs," in *Advances in Neural Information Processing Systems*, 2016, pp. 2234–2242.
- [32] T. Miyato, T. Kataoka, M. Koyama, and Y. Yoshida, "Spectral normalization for generative adversarial networks," in *International Conference on Learning Representations*, 2018, pp. 1–26.
- [33] I. Gulrajani, F. Ahmed, M. Arjovsky, V. Dumoulin, and A. C. Courville, "Improved training of Wasserstein GANs," in *Advances in Neural Information Processing Systems*, 2017, pp. 5769–5779.
- [34] M. Heusel, H. Ramsauer, T. Unterthiner, B. Nessler, and S. Hochreiter, "GANs trained by a two time-scale update rule converge to a local Nash equilibrium," in *Advances in Neural Information Processing Systems*, 2017, pp. 6629–6640.
- [35] A. Odena, C. Olah, and J. Shlens, "Conditional image synthesis with auxiliary classifier GANs," in *International Conference on Machine Learning*, 2017, pp. 2642–2651.
- [36] A. Nguyen, J. Clune, Y. Bengio, A. Dosovitskiy, and J. Yosinski, "Plug & play generative networks: Conditional iterative generation of images in latent space," in *IEEE/CVF Conference on Computer Vision and Pattern Recognition*, 2017, pp. 4467–4477.
- [37] H. Zhang, T. Xu, H. Li, S. Zhang, X. Wang, X. Huang, and D. N. Metaxas, "StackGAN: Text to photo-realistic image synthesis with stacked generative adversarial networks," in *International Conference on Computer Vision*, 2017, pp. 5907–5915.
- [38] S. Reed, Z. Akata, X. Yan, L. Logeswaran, B. Schiele, and H. Lee, "Generative adversarial text to image synthesis," in *International Conference on Machine Learning*, 2016, pp. 1060–1069.
- [39] S. Hong, D. Yang, J. Choi, and H. Lee, "Inferring semantic layout for hierarchical text-to-image synthesis," in *IEEE/CVF Conference on Computer Vision and Pattern Recognition*, 2018, pp. 7986–7994.
- [40] P. Isola, J.-Y. Zhu, T. Zhou, and A. A. Efros, "Image-to-image translation with conditional adversarial networks," in *IEEE/CVF Conference on Computer Vision and Pattern Recognition*, 2017, pp. 1125–1134.
- [41] Y. Song, J. Sohl-Dickstein, D. P. Kingma, A. Kumar, S. Ermon, and B. Poole, "Score-based generative modeling through stochastic differential equations," in *International Conference on Learning Representations*, 2021, pp. 1–36.
- [42] O. Ronneberger, P. Fischer, and T. Brox, "U-Net: Convolutional networks for biomedical image segmentation," in *Medical Image Computing and Computer-Assisted Intervention*, 2015, pp. 234–241.
- [43] J. Song, C. Meng, and S. Ermon, "Denoising diffusion implicit models," in *International Conference on Learning Representations*, 2020, pp. 1–20.
- [44] H. Zheng, W. Nie, A. Vahdat, K. Azizzadenesheli, and A. Anandkumar, "Fast sampling of diffusion models via operator learning," in *International Conference on Machine Learning*, 2023, pp. 42390–42402.
- [45] Y. Song, P. Dhariwal, M. Chen, and I. Sutskever, "Consistency models," in *International Conference on Machine Learning*, 2023, pp. 32211–32252.

- [46] T. Salimans and J. Ho, "Progressive distillation for fast sampling of diffusion models," in *International Conference on Learning Representations*, 2022, pp. 1–21.
- [47] X. Ma, G. Fang, and X. Wang, "DeepCache: Accelerating diffusion models for free," in *IEEE/CVF Conference on Computer Vision and Pattern Recognition*, 2024, pp. 15762–15772.
- [48] T. Karras, M. Aittala, T. Aila, and S. Laine, "Elucidating the design space of diffusion-based generative models," in *Advances in Neural Information Processing Systems*, 2022, pp. 26565–26577.
- [49] A. Shih, S. Belkhale, S. Ermon, D. Sadigh, and N. Anari, "Parallel sampling of diffusion models," in *Advances in Neural Information Processing Systems*, 2024, pp. 1–14.
- [50] D. Watson, W. Chan, J. Ho, and M. Norouzi, "Learning fast samplers for diffusion models by differentiating through sample quality," in *International Conference on Learning Representations*, 2022, pp. 1–17.
- [51] D. Podell, Z. English, K. Lacey, A. Blattmann, T. Dockhorn, J. Müller, J. Penna, and R. Rombach, "SDXL: Improving latent diffusion models for high-resolution image synthesis," *arXiv preprint arXiv:2307.01952*, 2023.
- [52] R. Rombach, A. Blattmann, D. Lorenz, P. Esser, and B. Ommer, "High-resolution image synthesis with latent diffusion models," in *IEEE/CVF Conference on Computer Vision and Pattern Recognition*, 2022, pp. 10684–10695.
- [53] A. Ramesh, P. Dhariwal, A. Nichol, C. Chu, and M. Chen, "Hierarchical text-conditional image generation with CLIP latents," *arXiv preprint arXiv:2204.06125*, 2022.
- [54] R. Durall, M. Keuper, and J. Keuper, "Watch your up-convolution: CNN based generative deep neural networks are failing to reproduce spectral distributions," in *IEEE/CVF Conference on Computer Vision and Pattern Recognition*, 2020, pp. 7890–7899.
- [55] S.-Y. Wang, O. Wang, R. Zhang, A. Owens, and A. A. Efros, "CNN-generated images are surprisingly easy to spot... for now," in *IEEE/CVF Conference on Computer Vision and Pattern Recognition*, 2020, pp. 8695–8704.
- [56] F. Marra, D. Gagnaniello, L. Verdoliva, and G. Poggi, "Do GANs leave artificial fingerprints?" in *Conference on Multimedia Information Processing and Retrieval*, 2019, pp. 506–511.
- [57] N. Yu, L. S. Davis, and M. Fritz, "Attributing fake images to GANs: Learning and analyzing GAN fingerprints," in *International Conference on Computer Vision*, 2019, pp. 7556–7566.
- [58] Y. Luo, J. Du, K. Yan, and S. Ding, "LaRE<sup>2</sup>: Latent reconstruction error based method for diffusion-generated image detection," in *IEEE/CVF Conference on Computer Vision and Pattern Recognition*, 2024, pp. 17006–17015.
- [59] J. Ricker, D. Lukovnikov, and A. Fischer, "AEROBLADE: Training-free detection of latent diffusion images using autoencoder reconstruction error," in *IEEE/CVF Conference on Computer Vision and Pattern Recognition*, 2024, pp. 9130–9140.
- [60] R. Ma, J. Duan, F. Kong, X. Shi, and K. Xu, "Exposing the fake: Effective diffusion-generated images detection," *arXiv preprint arXiv:2307.06272*, 2023.
- [61] B. Chen, J. Zeng, J. Yang, and R. Yang, "DRCT: Diffusion reconstruction contrastive training towards universal detection of diffusion generated images," in *International Conference on Machine Learning*, 2024, pp. 1–19.
- [62] B. Liu, F. Yang, X. Bi, B. Xiao, W. Li, and X. Gao, "Detecting generated images by real images," in *European Conference on Computer Vision*, 2022, pp. 95–110.
- [63] C. Tan, Y. Zhao, S. Wei, G. Gu, and Y. Wei, "Learning on gradients: Generalized artifacts representation for GAN-generated images detection," in *IEEE/CVF Conference on Computer Vision and Pattern Recognition*, 2023, pp. 12105–12114.
- [64] Y. Bengio, A. Courville, and P. Vincent, "Representation learning: A review and new perspectives," *IEEE Transactions on Pattern Analysis and Machine Intelligence*, vol. 35, no. 8, pp. 1798–1828, 2013.
- [65] C. Doersch, A. Gupta, and A. A. Efros, "Unsupervised visual representation learning by context prediction," in *International Conference on Computer Vision*, 2015, pp. 1422–1430.
- [66] S. Gidaris, P. Singh, and N. Komodakis, "Unsupervised representation learning by predicting image rotations," *arXiv preprint arXiv:1803.07728*, 2018.
- [67] M. Norouzi and P. Favaro, "Unsupervised learning of visual representations by solving jigsaw puzzles," in *European Conference on Computer Vision*, 2016, pp. 69–84.
- [68] N. Srivastava, E. Mansimov, and R. Salakhudinov, "Unsupervised learning of video representations using LSTMs," in *International Conference on Machine Learning*, 2015, pp. 843–852.
- [69] M. Caron, P. Bojanowski, A. Joulin, and M. Douze, "Deep clustering for unsupervised learning of visual features," in *European Conference on Computer Vision*, 2018, pp. 132–149.
- [70] T. Chen, S. Kornblith, M. Norouzi, and G. Hinton, "A simple framework for contrastive learning of visual representations," in *International Conference on Machine Learning*, 2020, pp. 1597–1607.
- [71] K. He, H. Fan, Y. Wu, S. Xie, and R. Girshick, "Momentum contrast for unsupervised visual representation learning," in *IEEE/CVF Conference on Computer Vision and Pattern Recognition*, 2020, pp. 9729–9738.
- [72] J.-B. Grill, F. Strub, F. Altché, C. Tallec, P. H. Richemond, E. Buchatskaya, C. Doersch, B. Á. Pires, Z. D. Guo, M. G. Azar, B. Piot, K. Kavukcuoglu, R. Munos, and M. Valko, "Bootstrap your own latent: A new approach to self-supervised learning," in *Advances in Neural Information Processing Systems*, 2020, pp. 21271–21284.
- [73] X. Chen and K. He, "Exploring simple Siamese representation learning," in *IEEE/CVF Conference on Computer Vision and Pattern Recognition*, 2021, pp. 15750–15758.
- [74] D. Pathak, P. Krahenbuhl, J. Donahue, T. Darrell, and A. A. Efros, "Context encoders: Feature learning by inpainting," in *IEEE/CVF Conference on Computer Vision and Pattern Recognition*, 2016, pp. 2536–2544.
- [75] G. Larsson, M. Maire, and G. Shakhnarovich, "Learning representations for automatic colorization," in *European Conference on Computer Vision*, 2016, pp. 577–593.
- [76] K. He, X. Chen, S. Xie, Y. Li, P. Dollár, and R. Girshick, "Masked autoencoders are scalable vision learners," in *IEEE/CVF Conference on Computer Vision and Pattern Recognition*, 2022, pp. 16000–16009.
- [77] A. Radford, J. W. Kim, C. Hallacy, A. Ramesh, G. Goh, S. Agarwal, G. Sastry, A. Askell, P. Mishkin, J. Clark, K. Gretchen, and S. Ilya, "Learning transferable visual models from natural language supervision," in *International Conference on Machine Learning*, 2021, pp. 8748–8763.
- [78] R. Arandjelovic and A. Zisserman, "Look, listen and learn," in *International Conference on Computer Vision*, 2017, pp. 609–617.
- [79] P. Vincent, H. Larochelle, Y. Bengio, and P.-A. Manzagol, "Extracting and composing robust features with denoising autoencoders," in *International Conference on Machine Learning*, 2008, pp. 1096–1103.
- [80] Z. Zhang, "A flexible new technique for camera calibration," *IEEE Transactions on Pattern Analysis and Machine Intelligence*, vol. 22, no. 11, pp. 1330–1334, 2000.
- [81] Y. Fang, H. Zhu, Y. Zeng, K. Ma, and Z. Wang, "Perceptual quality assessment of smartphone photography," in *IEEE/CVF Conference on Computer Vision and Pattern Recognition*, 2020, pp. 3677–3686.
- [82] J. Fan, H. Cao, and A. C. Kot, "Estimating EXIF parameters based on noise features for image manipulation detection," *IEEE Transactions on Information Forensics and Security*, vol. 8, no. 4, pp. 608–618, 2013.
- [83] L. L. Thurstone, "A law of comparative judgment," *Psychological Review*, vol. 34, pp. 273–286, 1927.
- [84] J. Su, M. Ahmed, Y. Lu, S. Pan, W. Bo, and Y. Liu, "Roformer: Enhanced Transformer with rotary position embedding," *Neurocomputing*, vol. 568, pp. 127063:1–127063:16, 2024.
- [85] B. Stojanoski and R. Cusack, "Time to wave good-bye to phase scrambling: Creating controlled scrambled images using diffeomorphic transformations," *Journal of Vision*, vol. 14, no. 12, pp. 6:1–6:16, 2014.
- [86] T. Foulsham, R. Alan, and A. Kingstone, "Scrambled eyes? Disrupting scene structure impedes focal processing and increases bottom-up guidance," *Attention, Perception, & Psychophysics*, vol. 73, pp. 2008–2025, 2011.
- [87] P. Li, J. Xie, Q. Wang, and Z. Gao, "Towards faster training of global covariance pooling networks by iterative matrix square root normalization," in *IEEE/CVF Conference on Computer Vision and Pattern Recognition*, 2018, pp. 947–955.
- [88] L. Van der Maaten and G. Hinton, "Visualizing data using t-SNE," *Journal of Machine Learning Research*, vol. 9, no. 11, pp. 2579–2605, 2008.
- [89] G. J. McLachlan and K. E. Basford, *Mixture Models: Inference and Applications to Clustering*. Marcel Dekker, 1988.

- [90] T. K. Moon, "The expectation-maximization algorithm," *IEEE Signal Processing Magazine*, vol. 13, no. 6, pp. 47–60, 1996.
- [91] M. De Lange, R. Aljundi, M. Masana, S. Parisot, X. Jia, A. Leonardis, G. Slabaugh, and T. Tuytelaars, "A continual learning survey: Defying forgetting in classification tasks," *IEEE Transactions on Pattern Analysis and Machine Intelligence*, vol. 44, no. 7, pp. 3366–3385, 2022.
- [92] T. Karras, S. Laine, and T. Aila, "A style-based generator architecture for generative adversarial networks," in *IEEE/CVF Conference on Computer Vision and Pattern Recognition*, 2019, pp. 4401–4410.
- [93] J.-Y. Zhu, T. Park, P. Isola, and A. A. Efros, "Unpaired image-to-image translation using cycle-consistent adversarial networks," in *International Conference on Computer Vision*, 2017, pp. 2223–2232.
- [94] Y. Choi, M. Choi, M. Kim, J.-W. Ha, S. Kim, and J. Choo, "StarGAN: Unified generative adversarial networks for multi-domain image-to-image translation," in *IEEE/CVF Conference on Computer Vision and Pattern Recognition*, 2018, pp. 8789–8797.
- [95] T. Park, M.-Y. Liu, T.-C. Wang, and J.-Y. Zhu, "Semantic image synthesis with spatially-adaptive normalization," in *IEEE/CVF Conference on Computer Vision and Pattern Recognition*, 2019, pp. 2337–2346.
- [96] T. Karras, S. Laine, M. Aittala, J. Hellsten, J. Lehtinen, and T. Aila, "Analyzing and improving the image quality of StyleGAN," in *IEEE/CVF Conference on Computer Vision and Pattern Recognition*, 2020, pp. 8110–8119.
- [97] J. West and C. Bergstrom, "whichfaceisreal," <https://www.whichfaceisreal.com/>, accessed: Mar 26, 2025.
- [98] A. Nichol, P. Dhariwal, A. Ramesh, P. Shyam, P. Mishkin, B. McGrew, I. Sutskever, and M. Chen, "GLIDE: Towards photorealistic image generation and editing with text-guided diffusion models," in *International Conference on Machine Learning*, 2022, pp. 16784–16804.
- [99] "WUKONG," <https://xihe.mindspore.cn/modelzoo/wukong>, accessed: Mar 26, 2025.
- [100] B. Thomee, D. A. Shamma, G. Friedland, B. Elizalde, K. Ni, D. Poland, D. Borth, and L.-J. Li, "YFCC100M: The new data in multimedia research," *Communications of the ACM*, vol. 59, no. 2, pp. 64–73, 2016.
- [101] J. Deng, W. Dong, R. Socher, L.-J. Li, K. Li, and L. Fei-Fei, "ImageNet: A large-scale hierarchical image database," in *IEEE/CVF Conference on Computer Vision and Pattern Recognition*, 2009, pp. 248–255.
- [102] F. Yu, A. Seff, Y. Zhang, S. Song, T. Funkhouser, and J. Xiao, "LSUN: Construction of a large-scale image dataset using deep learning with humans in the loop," *arXiv preprint arXiv:1506.03365*, 2015.
- [103] Z. Liu, X. Qi, and P. H. Torr, "Global texture enhancement for fake face detection in the wild," in *IEEE/CVF Conference on Computer Vision and Pattern Recognition*, 2020, pp. 8060–8069.
- [104] Y. Ju, S. Jia, L. Ke, H. Xue, K. Nagano, and S. Lyu, "Fusing global and local features for generalized AI-synthesized image detection," in *International Conference on Image Processing*, 2022, pp. 3465–3469.
- [105] C. Tan, Y. Zhao, S. Wei, G. Gu, P. Liu, and Y. Wei, "Rethinking the up-sampling operations in CNN-based generative network for generalizable deepfake detection," in *IEEE/CVF Conference on Computer Vision and Pattern Recognition*, 2024, pp. 28130–28139.
- [106] Black Forest Labs, "Flux.1: A new era of creation," <https://blackforestlabs.ai/>, accessed: Nov 19, 2025.
- [107] stability.ai, "Introducing stable diffusion 3.5," <https://stability.ai/news/introducing-stable-diffusion-3-5/>, accessed: Nov 19, 2025.
- [108] C. Wu, J. Li, J. Zhou, J. Lin, K. Gao, K. Yan, S.-m. Yin, S. Bai, X. Xu, Y. Chen *et al.*, "Qwen-image technical report," *arXiv preprint arXiv:2508.02324*, 2025.
- [109] T.-Y. Lin, M. Maire, S. Belongie, J. Hays, P. Perona, D. Ramanan, P. Dollár, and C. L. Zitnick, "Microsoft COCO: Common objects in context," in *European Conference on Computer Vision*, 2014, pp. 740–755.
- [110] "Tongyi," <https://tongyi.aliyun.com/wan/explore>, accessed: Sep 26, 2025.
- [111] "Lummi," <https://www.lummi.ai/>, accessed: Sep 26, 2025.
- [112] Y. Zheng, Y. Zhao, M. Ren, H. Yan, X. Lu, J. Liu, and J. Li, "Cartoon face recognition: A benchmark dataset," in *ACM International Conference on Multimedia*, 2020, pp. 2264–2272.
- [113] P. Shaw, J. Uszkoreit, and A. Vaswani, "Self-attention with relative position representations," in *North American Chapter of the Association for Computational Linguistics: Human Language Technologies*, 2018, pp. 464–468.
- [114] J. G. Daugman, "Uncertainty relation for resolution in space, spatial frequency, and orientation optimized by two-dimensional visual cortical filters," *Journal of the Optical Society of America A*, vol. 2, no. 7, pp. 1160–1169, 1985.
- [115] M. Zou, N. Zhong, B. Yu, Y. Zhan, and K. Ma, "Bi-level optimization for self-supervised AI-generated face detection," in *International Conference on Computer Vision*, 2025, pp. 18959–18968.